GOLD OA

OPEN ACCESS

THE GEOLOGICAL SOCIETY OF AMERICA®

Zircon age spectra to quantify magma evolution

A.K. Schmitt[1,2,3], J. Sliwinski[4,5], L. Caricchi[6], O. Bachmann[4], N. Riel[2,7], B.J.P. Kaus[2,7], A. Cisneros de Léon[8], J. Cornet[4], B. Friedrichs[9], O. Lovera[10], T. Sheldrake[6], and G. Weber[11]

[1]Institute of Earth Sciences, Heidelberg University, Im Neuenheimer Feld 234–236, 69120 Heidelberg, Germany
[2]Terrestrial Magmatic System Research Center (Universities of Mainz, Heidelberg, and Frankfurt), Germany
[3]John de Laeter Centre, Curtin University, Kent Street, Bentley, Western Australia 6102, Australia
[4]Institute of Geochemistry and Petrology, Department of Earth Sciences, ETH Zurich, Clausiusstrasse 25, 8092 Zurich, Switzerland
[5]School of Earth and Environmental Sciences, University of St. Andrews; Queen's Terrace, St. Andrews KY16 9TS, UK
[6]Department of Earth Sciences, Rue des Maraichers 13, 1205 Geneva, Switzerland
[7]Institute of Geosciences, Johannes-Gutenberg-University Mainz, Johann-Joachim-Becher-Weg 21, 55099 Mainz, Germany
[8]School of the Earth, Ocean and Environment, University of South Carolina, 701 Sumter Street, EWS 617, Columbia, South Carolina 29208, USA
[9]Department of Environment & Biodiversity, Paris Lodron University Salzburg, Hellbrunner Straße 34, 5020 Salzburg, Austria
[10]Department of Earth, Planetary, and Space Sciences, University of California, 595 Charles Young Drive, Los Angeles, California 90095, USA
[11]Department of Earth Sciences, University of Oxford, Oxford OX1 3AN, UK

ABSTRACT

The past decades have seen tremendous advances in analytical capabilities regarding the sensitivity, spatial selectivity, and instrumental precision of U-Th-Pb zircon geochronology. Along with improved zircon pretreatment to mitigate the effects of Pb-loss, these advancements have resulted in the emergence of U-Th-Pb dating as the most widely used geochronometer. In parallel, it became increasingly obvious that modern analytical techniques can resolve zircon age dispersal beyond instrumental uncertainties and that this dispersion cannot be attributed to Pb-loss or inheritance. Hence, there is a pressing need to refine statistical procedures for displaying and interpreting dispersed age data from volcanic and plutonic rocks, where zircon ages were traditionally assigned to the quasi-instantaneous events of eruption and magma emplacement, respectively. The ability to resolve zircon age spectra, which often range over timescales of 10^3–10^6 years, also offers new opportunities to monitor magmatic processes, because zircon crystallization directly relates to the temperature and composition of its host melt. This relation is, at least for typical subalkaline melt compositions, well calibrated by multiple zircon saturation experiments, although absolute saturation temperatures derived from them can vary by tens of degrees. Moreover, zircon saturation thermometry is supported by the trace element and isotopic inventory of zircon, which records the thermochemical and compositional evolution of melts at high fidelity. Here, we first review the properties of true zircon age spectra that are defined by a statistically robust overdispersion relative to analytical uncertainties. Secondly, we evaluate existing models and present new models that aim to quantitatively translate the properties of zircon age spectra into parameters controlling the longevity and thermal evolution of crustal magma bodies such as magma recharge flux and duration. These developing approaches, which aspire to capture all processes that affect the formation and dispersal of zircon in dynamic crustal magma systems, have the potential to foster an improved understanding of magmatism with implications for volcanic hazard assessment, geothermal energy uses, and the origins of ore deposits.

■ 1 INTRODUCTION: SCOPE OF THIS REVIEW

Zircon geochronology is the gold standard for defining the geologic timescale (e.g., Schaltegger et al., 2015; Schoene, 2014). The U-Th-Pb system in zircon, including the chronometer based on intermediate decay chain isotopes ^{230}Th and its indirect parent, ^{238}U, ranks nominally at the top of closure temperatures for geochronology, whereby the dissolution of zircon typically outpaces the diffusive mobilization of parent and daughter isotopes within crystalline zircon at reasonable temperatures and timescales for crustal magmatic systems (Cherniak and Watson, 2001). Hence, U-Th-Pb zircon dates can be straightforwardly interpreted as recording its crystallization in zircon-saturated melts (e.g., Watson and Harrison, 1983), although zircon can also form in metamorphic and hydrothermal environments (e.g., Kohn et al., 2015; Schaltegger, 2007). Three main zircon geochronology methods are used, and each has its individual strengths and limitations (Table 1). Isotopic analysis of U-Th-Pb in zircon by isotope dilution–thermal ionization mass spectrometry (ID-TIMS) is now achieved at <0.1% relative age uncertainty for single crystals or µg-sized fragments (e.g., Schaltegger et al., 2015) because of the routine pretreatment of zircon by chemical abrasion (CA), which successfully mitigates the effects of Pb-loss due to metamictization (e.g., Kryza et al., 2012; Mattinson, 2005; von Quadt et al., 2014). These improvements were paralleled by progress in high spatial resolution analysis at the scale of subgrain domains (with <1 ng material consumed) using laser ablation–inductively coupled plasma–mass spectrometry (LA-ICP-MS), and at even higher spatial resolution with secondary ionization mass spectrometric (SIMS) techniques (Table 1). U-Pb zircon geochronology has a lower limit for precise age determination due to a

A.K. Schmitt ⬤ https://orcid.org/0000-0002-9029-4211

TABLE 1. COMPARISON OF ROUTINE GEOCHRONOLOGICAL METHODS APPLIED TO ZIRCON IN ORDER OF DECREASING SAMPLE CONSUMPTION AND HENCE RISK FOR CONVOLUTION OF AGE DOMAINS

	Isotope dilution–thermal ionization mass spectrometry (ID-TIMS)	Laser ablation–inductively coupled plasma–mass spectrometry (LA-ICP-MS)	Secondary ion mass spectrometry (SIMS)
Relative analytical precision and achievable absolute age resolution (2σ)	U–Pb ≤0.1%; ~10^3–10^4 yr at 1–10 Ma; U–Th impractical due to multi-grain sample requirement	U–Pb and U–Th ~2%; ~10^3–10^4 yr for U–Th at <<300 ka	U–Pb and U–Th ~1–2%; ~10^3–10^4 yr for U–Th at <<300 ka
Spatial resolution	Single crystals or fragments analyzed with mixing of age domains	Spot analysis with ~20–30 µm diameter and ~10–20 µm depth	Spot analysis with ~20–30 µm diameter and ~1–5 µm depth; sub-µm resolution in depth profiling
Theoretically resolvable age difference*	~3×10^4 yr for radial growth of 30 µm	~9×10^3 yr for 10 µm depth	~9×10^2 yr for 1 µm depth
Sample preparation	Grain separates	Mounts with sectioned or unsectioned grains; in-situ	Mounts with sectioned or unsectioned grains; in-situ
Targeting aids†	CL imaging possible, but results in loss of crystal available for bulk analysis	Targeting after CL imaging	Targeting after CL imaging (except for depth profiling)
Time requirements	Time-consuming digestion and chemical separation prior to mass spectrometric analysis	Fast volumetric excavation rate (~10 µm³/s at ~2 J/cm⁻² fluence); ~2–3 min per analysis	Slow volumetric excavation rate (~0.1 µm³/s/nA primary beam); ~10–20 min per analysis

Notes: Table modified from Schaltegger et al. (2015).
*Based on a radial zircon growth rate of 3.6×10^{-15} cm/s (Storm et al., 2012); faster growth rates and therefore briefer resolvable age differences are possible, e.g., in high-temperature or alkaline melts.
†CL—cathodoluminescence; note that other non-destructive imaging methods are potentially useful, such as backscattered electron, Micro-Raman, or Time-of-Flight (TOF) SIMS mapping.

combination of low radiogenic signals and required corrections for initial disequilibrium in the U decay chains (e.g., Schaltegger et al., 2015). Extending accessory mineral geochronology into the Holocene requires application of U-series methods, in which disequilibrium between ^{230}Th and its indirect parent, ^{238}U, is measured (U-Th geochronology). The absolute age resolution for the U-Th method, however, diminishes when approaching secular equilibrium, which effectively limits its applicability to zircon of <300 ka (e.g., Schmitt, 2011). Applying these methods, sometimes in combination, has increasingly helped to resolve complex crystallization histories and inheritance in zircon, whereby the highest absolute age precision is achievable in samples of young age and/or by the analytically most precise method (Table 1).

The general expectation of most geochronology users is that applying any of these different and often complementary methods to zircon will lead to a well-defined age—the equivalent of a point on the time axis (Fig. 1)—where assigned uncertainties only reflect the analytical and systematic uncertainties of the method (e.g., uncertainties in isotope ratio measurements, and decay constant errors, respectively). This age may then be interpreted as corresponding to a specific geologic event, such as the eruption of a volcanic rock (Fig. 1) or magma emplacement of a plutonic rock, with these events being thought to have happened faster than the timespan indicated by stated uncertainties. Uncertainties can be further reduced by averaging results from replicate analyses of individual crystals and/or spots from the same sample or closely related samples. Normally distributed ages from replicate analyses are generally vetted using the reduced chi-square statistics, with the mean square of weighted deviates (MSWD) expressing the degree of dispersion of analyses around an average relative to the magnitude of the analytical errors. Data sets in which the MSWD is within acceptable limits of unity are reasonably interpreted to be derived from the same normal distribution. In this case, the uncertainty for the age is the standard error, i.e., the standard deviation divided by the square root of the number of analyses. Averaging replicate analyses results in much improved precision compared to the individual ages (e.g., Crowley et al., 2007). Data sets with MSWD values >>1 indicate data dispersion exceeding what is explainable by analytical uncertainties alone. These are often interpreted as either affected by Pb-loss or zircon inheritance, which leads to younger and older ages in a population, respectively.

With increased analytical precision and improved spatial selectivity of available geochronological methods, however, zircon dates even from hand sample-sized volcanic or plutonic rocks often display a spectrum of ages rather than defining a point in time. Zircon age spectra thus result from dates being distributed over a time interval in which at least the extremes are distinctly resolved beyond analytical uncertainties. Age overdispersal relative to analytical uncertainties ranging between 10^3 years and >10^6 years has been documented for both U-Th disequilibrium and U-Pb geochronometers at different timescales, and it is found regardless of the analytical method applied (TIMS, LA-ICP-MS, and SIMS) or the geological environment of the sample (e.g., for volcanic and plutonic zircon). Examples are detailed in section 2.6 below. The veracity of zircon age spectra is also upheld if stringent criteria for identifying potential Pb-loss or unrecognized inheritance (i.e., the incorporation of recycled zircon typically from wall rocks) are upheld, although both effects are certainly relevant for ancient zircon, or for some TIMS dates due to the larger crystal volume sampled using TIMS as compared to LA-ICP-MS or SIMS (e.g., Schaltegger et al., 2015). Furthermore, smoking-gun evidence against zircon age spectra being simply caused by unrecognized Pb-loss or inheritance comes from the U-Th zircon geochronology of late Pleistocene–Holocene volcanic rocks, which are too young to
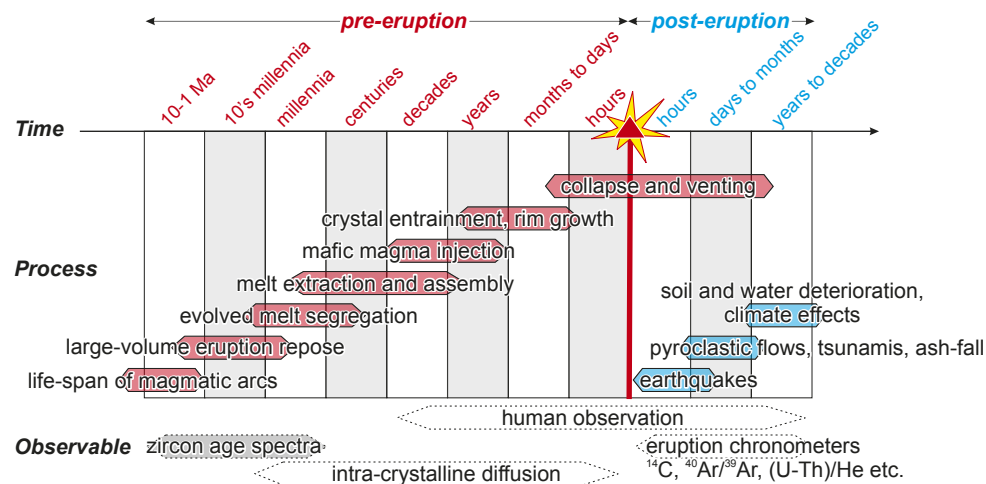
Figure 1. Schematic compilation contrasting a geological event illustrated by the eruption of an island arc volcano with the processes occurring before and after this event (pre- and post-eruptive) and their respective timescales (modified after Flaherty et al., 2018). Potential observables for reconstructing these processes are shown with their respective temporal resolution. Zircon age spectra in volcanic and plutonic rocks are useful for processes operating at 10^3 to $>10^6$ year timescales, whereas diffusion modeling of crystals can bridge these timescales with those accessible by direct human observation (e.g., through geophysical monitoring of active volcanoes). Instead of an eruption, magma extraction and intrusion would be an alternative scenario for geologically fast events, although a more inconspicuous one.

be affected by metamictization, and where U decay products, including ^{230}Th, are essentially immobile in the crystal lattice (Cherniak et al., 1997). Thus, post-crystallization disturbance can be ruled out for young zircon crystals, and spatially selective analysis (e.g., through SIMS depth profiling) can distinguish growth domains at the micrometer scale that show significant rimward younging. Zircon growth rates (Table 1) have been determined by this method (e.g., Storm et al., 2012; Friedrichs et al., 2021).

Thus, it has become evident over the past 25 years or so that zircon crystallization in magmas must be conceptualized as prolonged rather than instantaneous, and this may significantly predate a volcanic eruption or emplacement of a shallow intrusion (Fig. 1; Reid et al., 1997). This has severe implications for interpreting the timing of a geological event such as a volcanic eruption from zircon age data, especially when compared to low closure temperature chronometers such as

^{40}Ar/^{39}Ar (Fig. 1; e.g., Oberli et al., 1990; Keller et al., 2018). In this regard, the resulting zircon age spectra in magmatic rocks are analogous to those found in sedimentary rocks, and for interpreting the geologic significance of these heterogeneous ages, igneous petrologists face problems similar to those of sedimentologists attempting to extract depositional ages and information on provenance from detrital zircon data (e.g., Coutts et al., 2019). Notable exceptions are (per-)alkaline magmas, where zircon solubility is extremely high (e.g., Gervasoni et al., 2016) and zircon can crystallize rapidly (and sometimes even as millimeter-sized megacrysts) within the resolution of U-Th and U-Pb chronometers (Table 1). Such rocks display comparatively uniform zircon age distributions in individual samples, but not necessarily for different samples from the same volcano (e.g., Campi Flegrei: Fedele et al., 2006; Gebauer et al., 2014; Laacher See: Schmitt et al., 2010, 2017). Other cases where zircon crystallizes rapidly

involve high-temperature, mafic-to-intermediate magma compositions, where eruption temperatures are close to zircon saturation conditions (e.g., in mid-oceanic-ridge settings; Hayman et al., 2019; Schmitt et al., 2011). Nonetheless, even such zircon age data sets, when viewed system-wide instead of at the scale of an individual hand-sample, can be complex and indicative of protracted magmatic evolution (e.g., Schmitt et al., 2010).

Here, we review challenges in zircon geochronology to reliably interpret zircon age spectra in the context of the different methods by which they were generated. As our focus is primarily on magmatic systems, we largely disregard the possibility of subsolidus ("hydrothermal") zircon crystallization in this review (e.g., Troch et al., 2018) and refrain from any discussion of zircon crystallization during regional metamorphism; instead, we refer readers to excellent recent reviews (Kohn, 2016; Rubatto, 2017). Because zircon crystallization in magmas is directly linked to the thermochemical conditions of the melt that are faithfully recorded by zircon (e.g., Claiborne et al., 2006, 2010), zircon age spectra systematics, when properly understood, can reveal processes of magma migration, accumulation, and cooling timescales for natural systems at timescales unattainable by other methods (Fig. 1). Calvin Miller, to whom this themed issue is dedicated, pioneered the investigation of accessory minerals to gain insights into magmatic processes that operate at scales ranging from individual volcanoes or plutons to planetary crusts. In this tradition, zircon age spectra are increasingly harnessed to constrain the thermal history of magmatic systems and the long-term magma fluxes that sustain them (e.g., Caricchi et al., 2014, 2016; Ratschbacher et al., 2018; Friedrichs et al., 2021; Liu et al., 2021; Lukács et al., 2021; Tierney et al., 2016; Weber et al., 2020; Melnik et al., 2021; Angeles-De La Torre et al., 2023). Used in this sense, they are complementary to crystal-scale diffusion chronometers that provide magmatic timescale information if diffusion parameters are known, and which—unlike zircon—also can be applied to mafic rocks where zircon is commonly absent, but with absolute time information (Fig. 1; see Costa et al., 2020, for a recent review).

■ 2 REPRESENTATION AND PROPERTIES OF OVERDISPERSED ZIRCON AGES (AGE SPECTRA)

2.1 Basic Considerations and Histograms

Zircon crystallizes primarily upon cooling and differentiation of magma as first experimentally quantified by Watson and Harrison (1983). Because magmatic systems evolve dynamically, with magma reservoirs undergoing episodes of recharge and eruptive venting (e.g., Annen et al., 2006), thermal variability in these reservoirs over time and space is expected. At low temperature and in subalkaline melts, the kinetics of zircon dissolution are sluggish; short-lived prograde pulses and the associated chemical changes resulting from magma recharge only cause incomplete resorption (Watson, 1996). The propensity of zircon to survive such heating events is underscored by the preservation of rounded crystals in arc-volcanic rocks with bulk compositions and eruptive temperatures at which zircon is undersaturated (e.g., Weber et al., 2020). If not erupted, preexisting zircon, albeit potentially partially resorbed, can become the nucleus for renewed zircon crystallization during retrograde episodes (Szymanowski et al., 2020; Bindeman and Melnik, 2016). The shape of the natural distribution of zircon ages in individual samples thus can be highly variable, and it also will depend on the method applied to determine zircon ages (see section 3). Different approaches to visualizing zircon ages, especially those that are over-dispersed relative to analytical uncertainty, have been developed, and these are described in the next paragraph and sections 2.2–2.4.

Most intuitively, ages can be displayed in a histogram with individual analytical results assigned to discrete bins. The appeal of a histogram is its simplicity (the shape is only affected by the bin width) and the faithful reproduction of the data with a low risk of over-interpretation. However, the use of a single bin width (e.g., equivalent to the analytical uncertainty) for an entire distribution is precisely what makes data visualization difficult for large data sets that cover a comparatively large age range relative to analytical uncertainties.

Moreover, analytical uncertainties for young zircon are primarily controlled by low signal intensities, unlike older zircon crystals, where other sources of uncertainty affecting the results dominate, such as correction factors for isotopic mass fractionation in ID-TIMS or relative sensitivities in LA-ICP-MS and SIMS (e.g., Schaltegger et al., 2015; Schoene, 2014). Hence, uncertainties for young high-U zircon are often much smaller than those for low-U zircon. One should note that as the number of analyses, n, approaches infinity in a data set, the shape of a histogram converges with that of a continuous curve. However, time and cost are limiting factors for generating such high-n data sets; so, for most samples, an approach is required where an acceptable approximation can be extrapolated from a limited number of dates (e.g., $n = 20–100$). The generation of such an approximation can be achieved in multiple ways, and the resulting representation of zircon age spectra is dependent on several key assumptions (see section 2.5).

2.2 Probability Density Plots (PDP)

PDPs are another straightforward way to generate age spectra in addition to histograms. The age and uncertainty of each measurement provides the mean and standard deviation of a Gaussian distribution, and the sum of these overlapping Gaussian distributions generates the age spectrum; alternatively, the probabilities can be summed into a cumulative PDP. The utility of this approach, however, has been called into question if analytical uncertainties are invariable and small compared to the range of values in the data set. Vermeesch (2012) noted that PDPs can "punish" less precise measurements by under-representing such measurements in detrital spectra. Namely, the sampling of a zircon population with higher inherent error (e.g., due to lower U concentration) will generate a broader Gaussian distribution. Then, the PDP of this distribution will be correspondingly smoothed due to the higher uncertainties of the individual data points. For these reasons, PDPs are sometimes foregone in favor of kernel density estimates (KDEs).

2.3 Kernel Density Estimates (KDEs)

KDEs are similar to PDPs in basic principle: Each measurement is arranged into a distribution (referred to here as a "kernel," for which different shapes can be prescribed, including Gaussian), where the width of the distribution is not determined by the analytical uncertainty (as in PDPs), but by a "bandwidth" that is algorithmically adjusted based on point density and therefore variable across the age range. As noted by Vermeesch (2012), KDEs have advantages for provenance analysis using detrital zircon age spectra where analytical uncertainties and ages vary considerably.

Drawbacks of KDEs are the complexity of the formulas used and the potential for the arbitrary selection of bandwidths. Whereas histograms and PDPs are easily produced with minimal input parameters and subsequently easily reproduced by other researchers, KDE formulas are typically hidden from view and can vary in how users of the program (e.g., DensityPlotter; Vermeesch, 2012) adjust the bandwidth. For example, consider a synthetic bimodal data set with two prescribed peaks at 5 Ma and 7 Ma (7000 ages; Fig. 2A). A 250-point random sample of the population is selected, representing the collection of data from a much larger population. The algorithm of Botev et al. (2010) yields multiple peaks that actually represent noise in the original data set (Fig. 2B). The estimate of DensityPlotter (Vermeesch, 2012), with an adaptive kernel bandwidth, avoids such overinterpretation and faithfully reproduces the original population shape, which indicates that this is the algorithm of choice for KDEs (Fig. 2C). However, the most notable results of this demonstration are that (1) KDEs can be strongly model-dependent; (2) it is essential to report metadata with KDEs (e.g., constant versus adaptive bandwidths); and (3) the algorithm of Vermeesch (2012) appears to be suitable for modeling zircon age spectra with realistic uncertainties, provided that no major changes are introduced to the source code.

2.4 Radial and Abanico Plots

Another method of data visualization that is currently underutilized in U-Th-Pb zircon geochronology
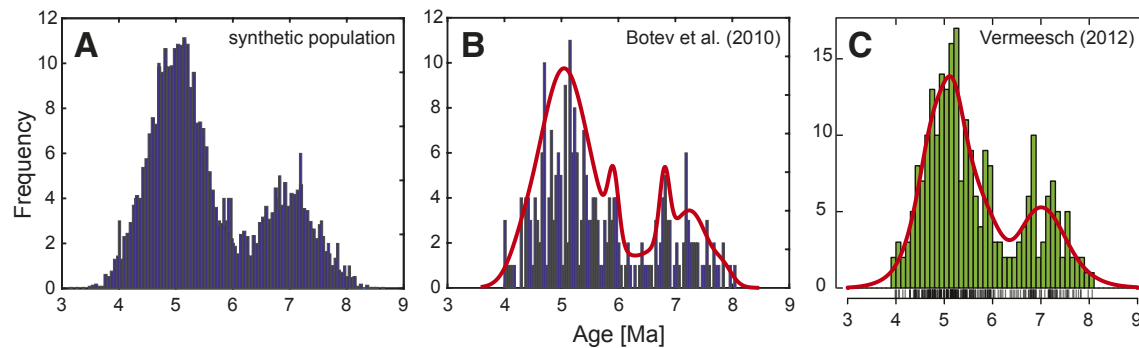
Figure 2. (A) A 7000-point synthetic data set with prescribed age peaks at 5 Ma and 7 Ma; (B) histogram of a 250-point random sample and a kernel density estimate (KDE) generated by the algorithm of Botev et al. (2010); (C) histogram of the same 250-point random sample as in part B, but using the algorithm of Vermeesch (2012) to generate a KDE that considers an adaptive kernel bandwidth. Note the differences in curve smoothing.

is the radial plot, which was introduced by Galbraith (1990) to represent fission-track data. Here, an additional dimension is added, allowing the user to visualize the amount of relative uncertainty on each data point on the *x*-axis, as well as the distribution of ages on the *y*-axis (Figs. 3B and 3C). Individual age peaks are calculated, as with KDEs (Fig. 3B), with the bonus that xenocrystic populations that may be difficult to spot in a histogram appear alongside the rest of the data at a lower point density (see Miller et al., 2007, for definitions of antecrystic and xenocrystic as used here). A modified version of this plot, the abanico plot (named after the Spanish term for a folding fan), includes a PDP on the right side of the graph (Vermeesch, 2012), combining properties of Figs. 3A and 3B.

The advantages of the radial plot being applied to magmatic zircon populations are, firstly, that the consideration of analytical uncertainty immediately informs the user about the relative value of each data point, decreasing the risk of overinterpretation even at a glance. Secondly, the existence of many zircon analyses of similar age but varying uncertainty works to create vectors in the radial plots that are easily differentiated from one another, and the slope of these vectors anchored at the origin indicates the age (marked along the radial part of the plot). Lastly, the addition of another data visualization method increases the confidence in the user's interpretation, particularly because the
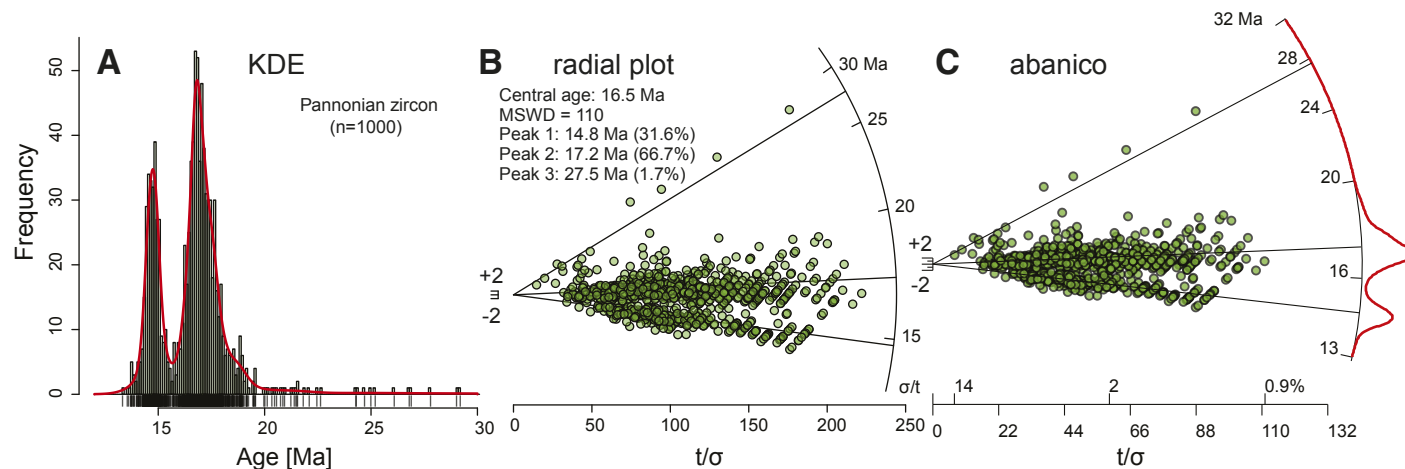

Figure 3. Comparison of plotting methods for the Pannonian zircon data set (Lukács et al., 2018): (A) histogram and kernel density estimate (KDE, red curve) of the data set, demonstrating a bimodal distribution; (B) radial plot after Galbraith (1990), where *x* values are plotted proportionally to 1/σ (uncertainty) and *y* values are determined from the deviation of each datum from a central value (e.g., a weighted average). All points on a line through the origin have the same age value that is denoted on the arc of a circle drawn at a convenient *x* value. The strong scatter demonstrates variability in data point uncertainties as a result of different measurement uncertainties (e.g., resulting from variably radiogenic Pb in young zircon); (C) abanico plot, with added probability density plot (PDP, red line on right), combining properties of a histogram and PDP/KDE curves as in part A with the data representation in part B.

interpretation of age spectra is only a semiquantitative method that requires a careful qualitative assessment as opposed to strict quantitation.

The attractiveness of the radial/abanico plot is that it easily and clearly captures the entire age spectrum, making it applicable to volcanic and plutonic zircon suites that may have a large xenocrystic component. This type of plot additionally excels at finding peaks of high sample density, which is particularly applicable to LA-ICP-MS/SIMS data sets. Application to TIMS data sets, on the other hand, is complicated by their relatively small size (typically <20 zircons) and high precision, which leads to the accentuation of individual zircon ages in a radial plot as opposed to a representative age of abundant zircon crystallization.

2.5 How Much is Enough? The Limits of Undersampling

The central supposition behind zircon age spectra analysis is that practical sampling of the zircon population (which is typically limited to tens to hundreds of zircons) still allows generation of an accurate representation of the true distribution. This is, however, far from trivial, because selection bias due to the method of zircon extraction (which may hinder, e.g., crystals included in phenocrysts from being liberated) or picking (where typically large, euhedral crystals are preferred) can hardly be avoided. With this caveat, we address the more tangible statistical problem of how many of the crystals that are available should be analyzed after a rock is subjected to a certain zircon identification and extraction procedure (Table 1). The larger the data set, the more accurate the representation of the true spectrum, but in practice, there are upper limits on the number that can be analyzed given time and cost considerations. The optimal size of n depends on (1) how many modes there are in a spectrum, as well as (2) the separation of the peaks and the analytical uncertainty, and (3) the model used to generate the spectral representation.

The number of modes in a zircon age distribution is effectively unconstrained, and the shape of a natural population will theoretically always appear spiky, provided there is sufficient temporal resolution (i.e., there could be as many age peaks as zircon crystals or crystal subdomains analyzed). One must therefore make a rough judgment about the number of crystals required to accurately capture the variability of their data set. For provenance analysis in sedimentary records (where age ranges may span billions of years), it is necessary to look at data sets numbering 100–1000+ zircons to resolve low-abundance age populations (Dodson et al., 1988; Pullen et al., 2014; Vermeesch, 2004). For magmatic studies, where the age range is much smaller, a data set of 100 zircons may encompass the natural variability of the population. A simple subsampling experiment demonstrates this concept (Fig. 4): Using subsamples of 20, 50, and 100 zircons from a data set of Miocene volcanic zircon crystals from Pannonia (Lukács et al., 2018), one can see that the overall variability of the entire data set is adequately captured by subsampling 50–100 zircons, which is
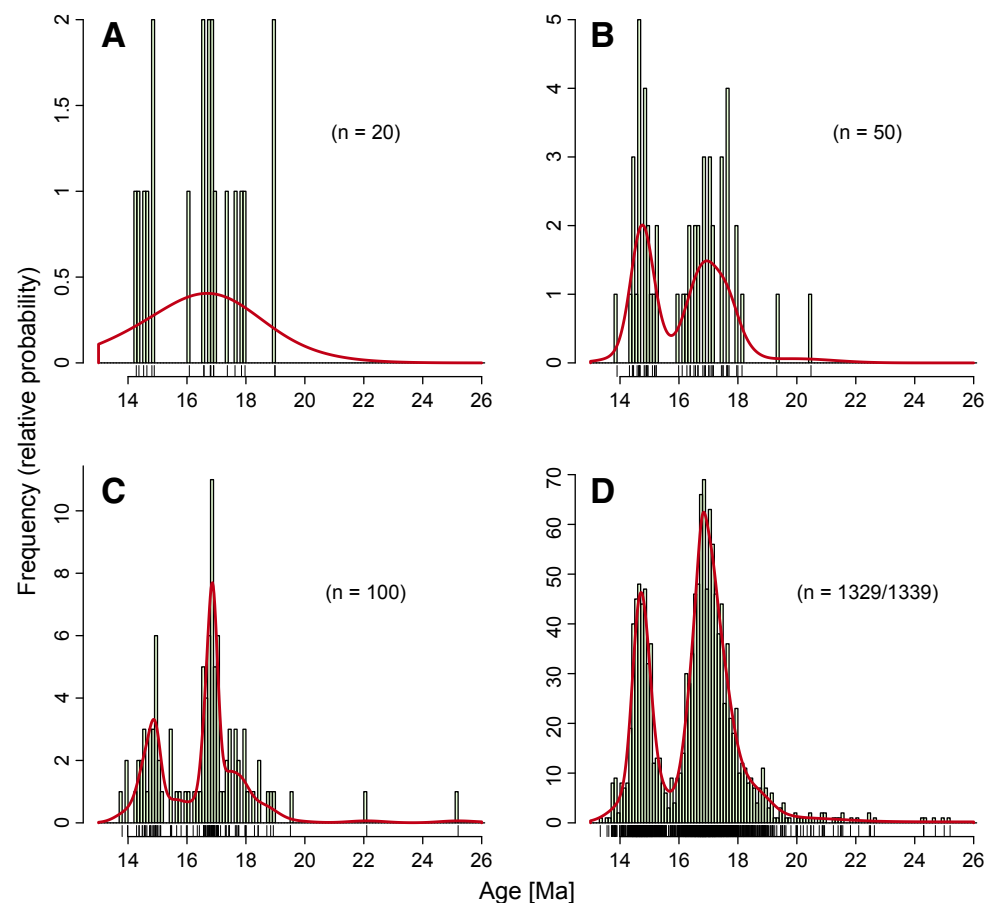

Figure 4. Histograms and corresponding kernel density estimate (KDE) plots demonstrating the effects of undersampling illustrated by subsampling of (A–C) 20, 50, and 100 zircons, respectively, from a data set of Miocene volcanic zircon crystals from Pannonia, compared to (D) the full population of 1339 zircons with 10 analyses plotting outside the range (Lukács et al., 2018). $^{206}Pb/^{238}U$ ages are plotted, with typical uncertainty of ca. 0.4 m.y., or ~3%.

in line with estimates from Caricchi et al. (2016). Here, the larger subsample also begins to resolve input from xenocrystic zircons at ca. 25 Ma as well as a shoulder in the data at ca. 18–19 Ma, which may reflect another population too close in age to be resolved by LA-ICP-MS. Importantly, small data sets (10–20 zircons) demonstrate no bimodality, which suggests that the KDE adequately protects against over-assigning individual peaks. For such small data sets, sampling only suggests an age of roughly 15–17 Ma (Figs. 4A and 4B). In larger subsamples, however, one can more confidently argue for the existence of two age peaks and perhaps identify different proportions of xenocrysts and the existence of subsidiary age peaks (Figs. 4C and 4D). However, these latter two interpretations should be considered strictly qualitative, and they require corroborating evidence. A statistically robust approach for identifying distinct populations in such mixtures was developed by Sambridge and Compston (1994) that is based on deconvolving multiple Gaussian peaks from a polymodal PDP.

The distance between age peaks (Δt) and analytical uncertainties plays a large role in determining whether age peaks can be resolved. Using the convention of a 95% confidence interval (abbreviated as 2σ, where σ refers to the standard error of an individual analysis; Table 1), it follows that for two age peaks to overlap at less than 5%, their separation must be at least 4σ (2σ for each peak). This is consistent with the Bayesian modeling of Keller et al. (2018), who determined that the ideal separation of age peaks should fall within the 3–5 σ range (i.e., Δt/σ = 3–5). In the previous example, with large age peaks at 14.8 Ma and 17.2 Ma and an analytical uncertainty amounting to ca. 0.7 Ma at the 4σ level (the mean of the 3–5σ range identified by Keller et al., 2018), the corresponding Δt of 2.4 Ma translates into a Δt/σ of ~14. The apparent shoulder at ca. 18.5 Ma presents a conundrum, however. While on the one hand, the Δt between this "peak" and the one at ca. 17.2 Ma is 1.3 Ma (well outside the 4σ criterion), the distribution appears to be continuous toward older ages, which suggests that this period experienced prolonged zircon crystallization and may in fact be composed of many smaller, and ultimately unresolvable, peaks. The test applied here

suggests that the minimal sample size for resolving bimodality in the Pannonian zircon example is ~50 zircon analyses, but reliable estimates of the percentage of each mode may require a larger number of analyses (e.g., 100; Fig. 4D). In the data set used here, the range between the modes is sufficiently large, and analytical uncertainties are sufficiently low. Under other circumstances, these criteria might not be met, and it is difficult to define a set of rules that applies universally, apart from two basic principles: (1) Δt/σ must be at least 3–5, and (2) a consistent algorithm that is commonly available must be used (e.g., Vermeesch, 2012).

Slightly different considerations hold for U-Th zircon ages, which cover an age range between ca. 0 ka and 300–350 ka. Because of the exponential relationship between isochron slope m (which for single zircon ages is usually defined by two points: the measured zircon composition and a constant model melt composition that is typically derived from U-Th whole-rock or glass analyses) and time, the absolute age uncertainty increases as secular equilibrium is approached. Kent and Cooper (2018) concluded that >100 zircon analyses are required to characterize U-Th zircon age spectra and to correctly interpret them in the context of a magma system's thermal history, but as ages approach secular equilibrium, the absolute age uncertainty, even for the same analytical precision, becomes too large to meaningfully distinguish different age populations. In favorable cases (e.g., high-radiogenic Pb yields), U-Pb geochronology can seamlessly complement U-Th ages.

2.6 True Zircon Age Spectra

Obtaining large zircon data sets is not always practical, especially for ID-TIMS geochronology, and we therefore showcase well-documented examples where zircon age spectra have been obtained at high-n sampling. To illustrate, we have summarized in Figs 5–8 PDPs, KDEs, and radial plots from four data sets of U-Pb and U-Th zircon data covering a wide age range. Data have been collected over the past few years at the University of California at Los Angeles/Heidelberg University (UCLA-HD) and ETH

Zürich using SIMS and LA-ICP-MS methods, respectively, and include: (1) The Belfond lava dome from the late Pleistocene Soufrière Volcanic Center (Saint Lucia, Lesser Antilles Arc); (2) the Miocene plutonic complex of La Gloria (Central Andes); (3) the Oligocene volcanic province of the Southern Rocky Mountains volcanic field (also previously called the San Juan volcanic field), western USA; and (4) the Ordovician plutonic complex of the Sierra de Famatina–Valle Fértil in NW Argentina.

The Soufrière Volcanic Center data (Fig. 5) comprise zircon from samples of the dacitic Belfond lava dome and cogenetic granodioritic enclaves that erupted at ca. 13.6 ka (Barboni et al., 2016; Schmitt et al., 2010). The data set includes zircon rim analyses of pristine growth surfaces, as well as interior analyses of sectioned crystals, but we do not differentiate between those in this comparison (cf. Schmitt et al., 2010). Lateral overlap of the ~30-μm-diameter ion beam used in SIMS analysis for crystal interior analyses could lead to mixed ages, whereas this is largely mitigated for the rim analyses in which the SIMS sputtering is parallel to the growth direction, integrating to a depth of <5 μm. Most of the Belfond zircon crystallization ages significantly predate the eruption age (dashed lines in Fig. 5) which was independently constrained by (U-Th)/He zircon dating. Interestingly, the dominant zircon age mode at ca. 28–29 ka is similar in the zircon populations of both the host lava and enclosed plutonic enclaves, which suggests recycling of zircon from crystal-rich domains of an intrusive reservoir during a younger magmatic episode (Fig. 5). These age modes predate the dome eruption by ~14 k.y. and the last major explosive eruption in the region at ca. 20 ka by ~8 k.y. Several minor peaks in decreasing abundance are present between ca. 40 ka and 114 ka, as well as some older crystals, in particular in the plutonic enclaves. The central age of the population (ca. 62 ka and 49 ka for lava and plutonic enclaves, respectively) has no geologic significance, but the significance of the older zircon crystals in terms of continuous versus punctuated crystallization is more difficult to distinguish, especially when the ion beam might have overlapped different growth domains (Fig. 5). The predominance of ages between ca. 40 ka and 114 ka, however, corresponds well with

major eruption pulses in the Soufrière Volcanic Center and a possible hiatus between ca. 250 ka and 110 ka, which again supports crystal recycling in a long-lived magma system (Schmitt et al., 2010).

La Gloria U-Pb zircon LA-ICP-MS data show a nearly Gaussian distribution, with a single peak at ca. 10.4 Ma (Fig. 5), which agrees within error with a published U-Pb zircon LA-ICP-MS age of 10.3 ± 0.2 Ma (Deckart et al., 2010). However, higher-precision ID-TIMS data on the same samples establish that the pluton crystallized zircons for almost 2 m.y., between 10.2 Ma and older than 12.0 Ma (Gutiérrez et al., 2018). Hence, it would be erroneous to interpret the relatively simple "unimodal" population seen by the LA-ICP-MS data as all zircon crystallizing during a single event corresponding to the weighted mean age of ca. 10.4 Ma. That such an interpretation is inadequate is also underscored by the elevated MSWD for the entire data set.

At even larger spatial and temporal scales than for individual volcanoes or plutons, zircon age spectra are also found for entire volcanic fields or arc segments. Geological background and additional age information is presented in the references provided, and here, we only summarize zircon ages from these cited studies. Large zircon age data sets for the Southern Rocky Mountains volcanic field (Sliwinski et al., 2022) and the Famatina Province show distinct peaks (Figs. 7 and 8). Again, both data sets display elevated MSWD values and central ages that lack any significance for dating a specific geological event. For the Southern Rocky Mountains volcanic field, two main peaks stand out at ca. 33–34 Ma and ca. 27–29 Ma that correspond to the peaks of activity in the northern and southern parts of the volcanic province, respectively. There is also a younger peak at ca. 23 Ma, which corresponds to the beginning of the Rio Grande Rift in the region, and the emplacement of some large silicic units (in particular, the Sunshine Peak Tuff that erupted at 22.93 ± 0.02 Ma; Lubbers et al., 2020; Mehnert et al., 1973).

For the Famatina region, there is a broad main peak, centered on an age of ca. 463 Ma, and a younger tail (<350 Ma) that may represent an episode of Carboniferous magmatism. However, as both the Southern Rocky Mountains volcanic field
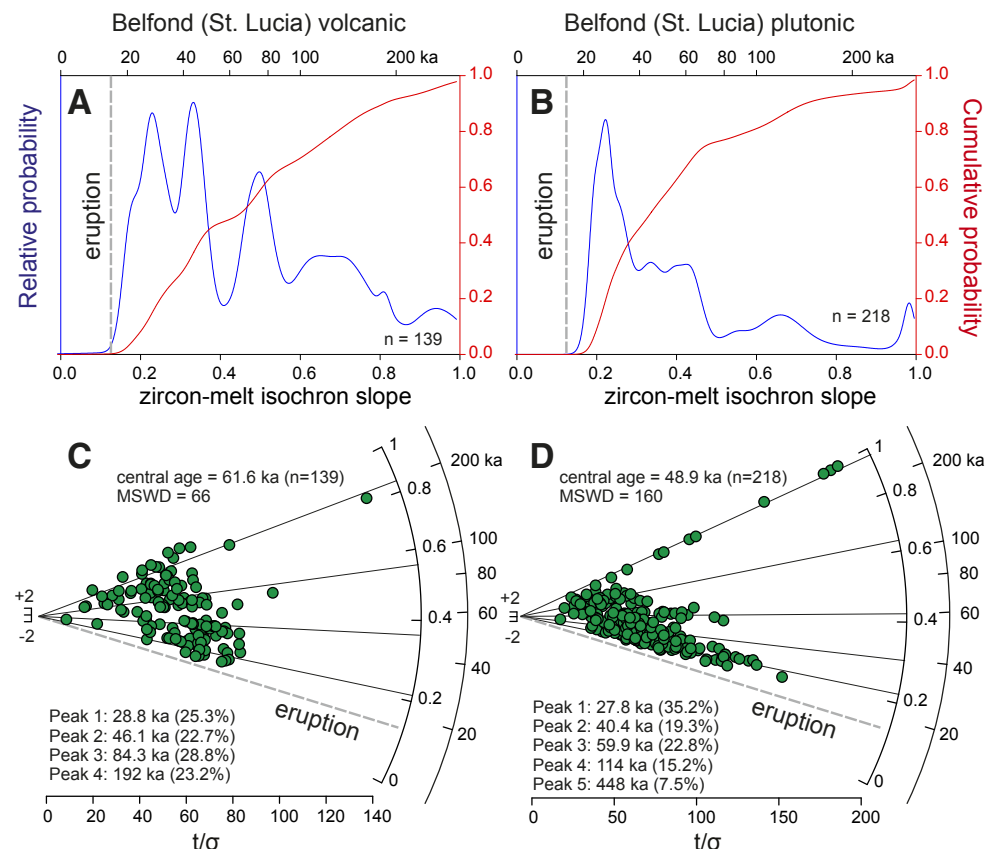
Figure 5. (A, B) Probability density plots (PDPs, with relative and cumulative probabilities in blue and red curves, respectively), and (C, D) radial plots (individual data points are in green). (A, C) Plots for U-Th zircon ages for volcanic and (B, D) plutonic samples of the Belfond lava dome, Soufrière Volcanic Center, St. Lucia (data were compiled from Schmitt et al., 2010, and Barboni et al., 2016). Bottom line in parts A and B and inner circle in parts C and D indicate the slope of the zircon-melt isochron using glass or whole-rock compositions as an anchor for the melt from which zircon crystallized (see Schmitt et al., 2010, and Barboni et al., 2016, for details). Dashed line marks the eruption age of the Belfond dome at 13.6 +0.45/−0.39 ka as independently determined by (U-Th)/He thermochronology (Schmitt et al., 2010). MSWD—mean square of weighted deviates.

and the Famatina regions are relatively old, the LA-ICP-MS uncertainties likely mask more complexity within the zircon age population. Based on high-precision ID-TIMS data, we know that zircon from single ignimbrite units of the Southern Rocky Mountains volcanic field has crystallization intervals on the order of 0.5–1 m.y., with potential zircon populations hidden within those peaks (e.g.,

Curry et al., 2021). Moreover, zircon ages systematically correlate with geochemical indicators such as Yb/Dy, which reflects accessory mineral saturation and hence the temperature evolution of the magma (Bachmann et al., 2007; Wotzlaw et al., 2013). Similarly, preliminary unpublished ID-TIMS data on some of the Famatinian units suggest peaks of zircon growth at ca. 475–480 Ma and ca. 465–470 Ma,
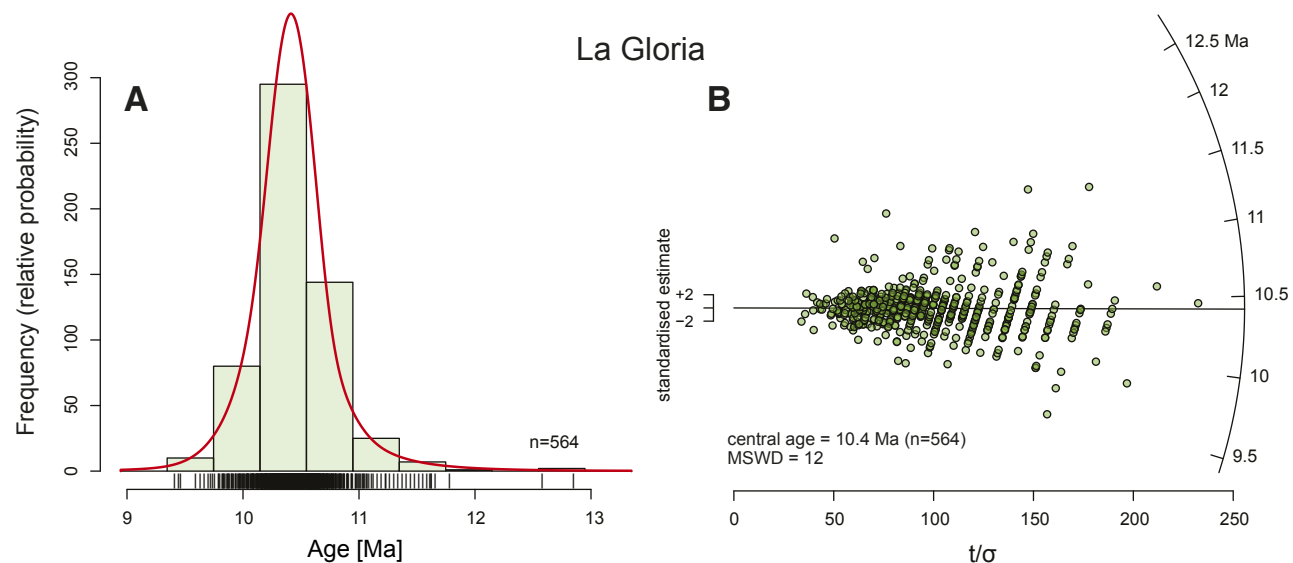
Figure 6. (A) Histogram and kernel density estimate (red curve) and (B) radial plot for U-Pb ages from La Gloria Pluton, Central Andes. The same data are plotted in parts A and B. MSWD—mean square of weighted deviates.
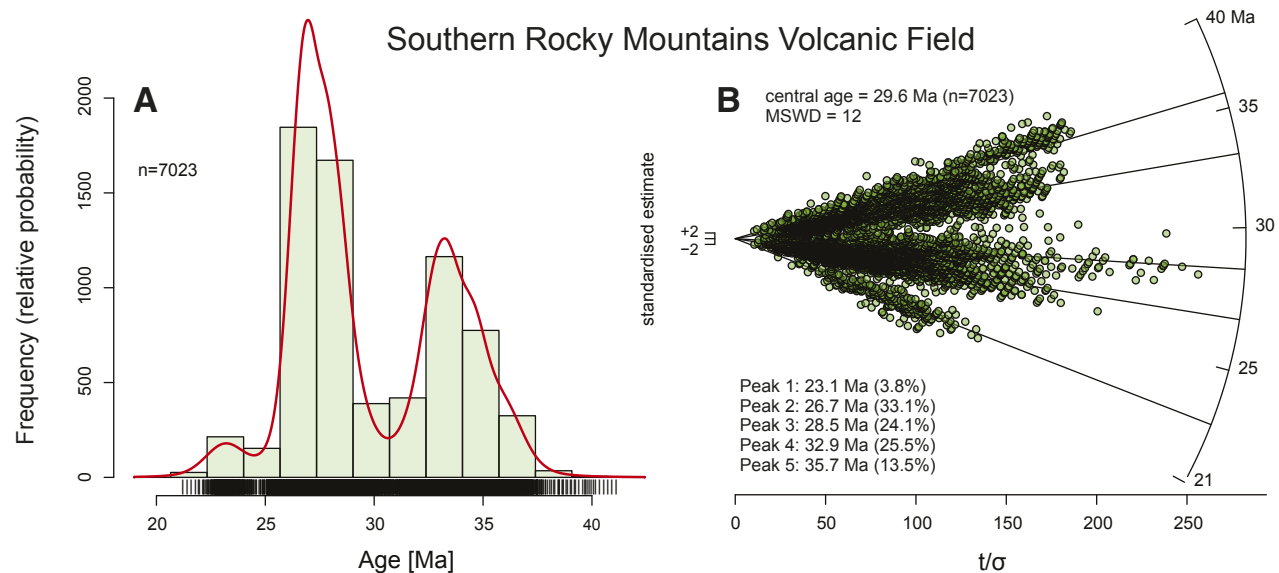

Figure 7. (A) Histogram and kernel density estimate (red curve) and (B) radial plot for U-Pb zircon ages from Southern Rocky Mountains Volcanic Field. The same data are plotted in parts A and B; data source is Sliwinski et al. (2022). MSWD—mean square of weighted deviates.
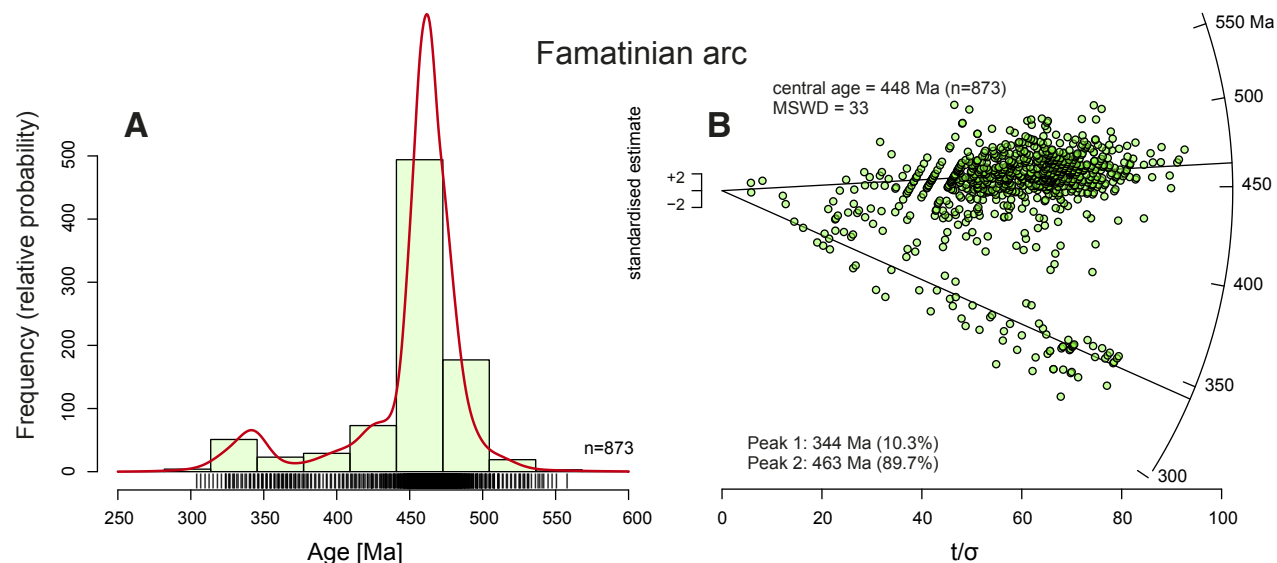
Figure 8. Histogram and kernel density estimate (red curve) and (B) radial plot for U-Pb zircon ages from the Famatinian arc. The same data are plotted in parts A and B. MSWD—mean square of weighted deviates.

hidden in the broad Ordovician peak of the comparatively low-precision LA-ICP-MS data. Hence, as pointed out in section 2.5 above, distinguishable events must be separated by >3–5σ to be isolated. With typical errors of ~1–2% (at 2σ) for U-Pb zircon LA-ICP-MS data, this means that igneous pulses for San Juan and Famatina need to be separated by more than 1–1.5 m.y. and 10–15 m.y., respectively, to be statistically distinguishable.

2.7 False Zircon Age Spectra

However, not every zircon age data set where excess scatter beyond analytical uncertainties exists (commonly inferred from an elevated MSWD value) should be considered a true zircon age spectrum. Sampling bias and analytical problems can produce excess scatter, and common issues are often specific to the analytical method applied. For example, even with chemical abrasion pretreatment, zircon domains that experienced Pb-loss may still contribute to an ID-TIMS analysis (e.g., Widmann et al., 2019).

Unrecognized inheritance, especially when xenocrystic contaminants are only marginally older than the magmatic episode, can also shift ID-TIMS dates to older ages (e.g., Widmann et al., 2019). Similar considerations hold for data from spatially selective methods, where CA pretreatment also shows promise but may not always be the silver bullet to eliminate zircon affected by Pb-loss (e.g., Kryza et al., 2012; Sliwinski et al., 2017; von Quadt et al., 2014).

Bias can also affect spatially selective methods: LA-ICP-MS dates are sensitive to fractionation corrections that depend on the depth of the ablation crater, and because ablation characteristics vary depending on the structural state of zircon, this may result in apparent age variability (Marillo-Sialer et al., 2016; Sliwinski et al., 2017). SIMS analysis of high-U zircon is known to yield apparent older ages when the relative sensitivity factor (RSF) is calibrated on normal-U zircon references (e.g., Schaltegger et al., 2015; White and Ireland, 2012). Lastly, assigning errors is model-dependent in all analytical methods, and not all sources of error are always identifiable. Thus, it is essential to monitor analytical performance by

analyzing matching secondary zircon references to identify potential under- or over-estimation of analytical error. Thus, we urge caution in invoking "protracted zircon crystallization" as a *carte blanche* for explaining away excess analytical scatter, particularly for geologically old igneous rocks, because the magmatic lifetimes typically observed for young volcanic systems are but a minor fraction of the overall analytical uncertainty. Analytical reliability, e.g., from analyzing homogeneous and well-characterized zircon references, is a prerequisite for identifying true zircon age spectra.

■ 3 UNDERSTANDING AND MODELING ZIRCON AGE SPECTRA TO EXTRACT INFORMATION ABOUT MAGMATIC SYSTEMS

3.1 Fundamentals and Modeling Rationale

In the second part of this review, we focus on existing and upcoming forward models to generate

distributions of zircon crystallization ages with the goal of quantifying rates and durations of magmatic input into volcanic plumbing systems (e.g., Caricchi et al., 2014, 2016; Friedrichs et al., 2021; Liu et al., 2021; Lukács et al., 2021; Tierney et al., 2016; Ratschbacher et al., 2018; Weber et al., 2020; Melnik et al., 2021). The main idea behind this modeling approach is to identify for which set of input parameters a computed zircon distribution—including age and possibly crystal age zonation as well as chemistry—is the closest to measured zircon from volcanic or plutonic rocks. These models are based on five tenets: (1) the thermal history of a magmatic intrusion can be adequately predicted, with reasonable assumptions regarding the shape of an igneous body (e.g., Annen et al., 2015); (2) zircon ages record magmatic crystallization; (3) zircon crystallizes between the zircon saturation temperature (T_{zr}) and the solidus temperature (T_s), and the zircon fraction per unit mass of magma decreases from T_{zr} to T_s according to an empirical zircon saturation model (e.g., Baker et al., 2002; Boehnke et al., 2013; Borisov and Aranovich, 2019; Gervasoni et al., 2016; Shao et al., 2020; Watson and Harrison, 1983); (4) the number of zircon crystals crystallizing in a magmatic plumbing system at each time interval is proportional to the change in the temperature distribution between T_{zr} and T_s; and (5) the fraction of measured zircon of different ages is representative of the proportions of zircon that crystallized within each age interval.

This last assumption deserves further comment, as the age distribution ultimately measured depends on the type of sample investigated (i.e., plutonic or volcanic) and the analytical method used (Table 1). Firstly, volcanic and plutonic zircons will sample different volumes and evolutionary stages of a magmatic system as plutonic zircons can grow in areas of very high crystallinity (and possibly hydrothermally at subsolidus conditions), whereas rheological thresholds for magma being able to erupt require that volcanic zircon is largely derived from the liquid-dominated part of a system at the time of eruption. As a telling example, basalt is typically devoid of zircons, but many gabbros contain zircon that crystallized interstitially from residual melt at near-solidus conditions (e.g., Hayman et al., 2019). Secondly, the analytical technique

used for dating can introduce bias (i.e., high spatial resolution on sectioned crystals in SIMS and LA-ICP-MS versus whole zircon by TIMS; Table 1). We first introduce these general concepts behind the modeling and then discuss the robustness of the critical assumptions in the following section (3.2).

To explain the fundamentals of the modeling approach, we can consider the simple case of a

spherical magmatic intrusion cooling at depth (Fig. 9) before addressing more complicated but realistic scenarios in which a magma system undergoes recharge. In the simplest case, magma is injected instantaneously at its liquidus temperature, (T_0), and the intrusion cools starting from its outer portions. Zircon crystallizes between T_{zr} down to T_s, and the rate of zircon crystallization either decreases
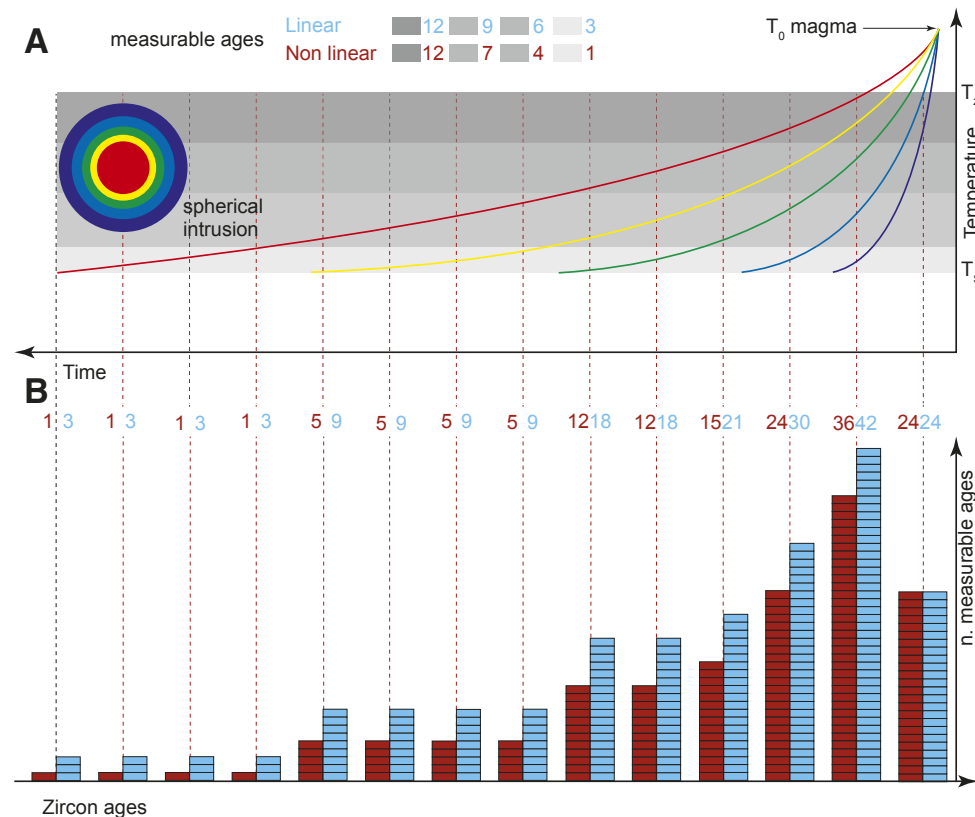

Figure 9. Schematic representation of the temporal evolution of temperature and measurable zircon crystallization ages within a spherical intrusion where each temperature interval has a randomly prescribed number of measurable zircon crystals (cyan and red numbers in part A). (A) Curves of different colors show the evolution of temperature within the reservoir portion with the corresponding color (inset). Gray shadings indicate different temperature intervals within which zircons crystallize at different rates (as shown in the legend for two models of zircon crystallization, linear and nonlinear). For nonlinear, we presume that with decreasing temperature there is an exponential decrease in the number of zircons crystallizing per unit time, as suggested by zircon saturation models. For the linear model, zircon crystallization rates simply decrease linearly with temperature. (B) Schematic distributions of measurable zircon ages resulting from cooling of the spherical reservoir and considering a linear (cyan) and nonlinear (red) zircon crystallization model.

linearly or (more realistically) exponentially with temperature (Fig. 9A). The exponentially decaying mass fraction of zircon is consistent with zircon saturation calibrations, where ~40% of the total amount of zircon that can form in a batch of magma crystallizes within 25 °C below the onset of zircon saturation, and only <10% crystallizes over the last 25 °C before reaching the solidus temperature (Harrison et al., 2007). Several observations can be made from this simple scenario. The distributions of ages calculated assuming linear or nonlinear (exponential) relationships between T and the amount of zircon crystallized differ, with linear models slightly overrepresenting younger zircon crystals compared to the nonlinear (exponential) model (Fig. 9B). In the absence of dynamic processes such as convection, the age distributions in the different portions of a solidified intrusion would be different, and the age of the youngest measurable zircon would decrease from the outer to the inner portions of the intrusion (Fig. 9B). If, hypothetically, the different shells were dynamically mixed prior to eruption (e.g., due to recharge and remobilization; Bachmann and Bergantz, 2006; Huber et al., 2009), a volcanic rock could contain a mix of all ages and different compositions (e.g., Pamukçu et al., 2022).

Considering a geologically more plausible system assembled by the injection of discrete pulses (e.g., Coleman et al., 2004), a zircon age distribution that is noticeably different from the previous scenario must be expected (Fig. 10). Importantly, the calculated distribution of measurable zircon ages would also look different if instead of considering the time-temperature paths of different portions of the intrusion, we were to only track the evolution of the average temperature. This implies that zircon age distributions calculated using an "average" time-temperature path cannot be used to retrieve reliable information about the thermal evolution of magmatic systems assembled by episodic magma injection (Figs. 10A and 10B).

The type of sample under investigation is also relevant, as zircon age distributions from plutonic or volcanic rocks will not have the same characteristics. For instance, if an eruption occurs during the assembly of a crustal magma reservoir, zircon sampled by the eruption will record a shorter age range

with respect to zircon collected from the solidified magma reservoir (Fig. 10B versus Fig. 10C). An exception could result from the remelting of a completely solidified portion of the reservoir, thus releasing its zircon cargo to the melt. The zircon age distributions in plutonic and volcanic rocks are different because an eruption must occur before the full solidification of a magmatic reservoir, and therefore the youngest measurable age in volcanic zircons must be older than the youngest measurable age in plutonic zircon. Additionally, some of the injected magma continuously cools below the solidus during assembly of a magmatic reservoir (e.g., Annen, 2009; Annen et al., 2006, 2015; Karakas et al., 2017), and zircon locked within the solidified portion of the magmatic system is less likely to be sampled by an eruption (e.g., Shane et al., 2012). Finally, zircon ages determined by bulk analysis techniques such as TIMS are average ages that record integrated down-temperature zircon crystallization from a zircon-saturated melt that may have lasted longer than analytical uncertainties indicate (Table 1). High spatial resolution ages from LA-ICP-MS and SIMS analyses, by contrast, permit the resolution of different stages of the magma's thermal history at 10^3–10^4 year intervals (Table 1). The example introduced earlier in this section of a single batch of magma cooling in a thermally uniform crustal environment is of course unrealistically simplified, as long-lived magmatic systems are sustained by frequent magmatic recharge. Thermal models for such systems that are open for recharge exist, but different approaches are rarely vetted against one another. Two of these models that are in use at the University of Geneva and UCLA-HD are therefore described here in detail to assess their similarities and differences regarding the inferred magmatic thermal history and to compare their predictions for zircon age spectra, primarily in volcanic settings.

3.2 Thermal Models for Magmatic Systems Undergoing Repeated Recharge

There has been a long tradition of modeling the thermal evolution of magmatic systems following

the repeated intrusion of dike- or sill-shaped magmatic batches. In these models, dikes or sills are kinematically inserted into a model space while moving host rocks to accommodate magmatic input, and the subsequent thermal evolution of the crust is monitored while taking partial melting and effects such as latent heat into account (e.g., Dufek and Bergantz, 2005; Annen et al., 2006; Caricchi et al., 2014; Tierney et al., 2016; Ratschbacher et al., 2018; Weber et al., 2020; Melnik et al., 2021). All models show that the first injections cool rapidly and a certain time is required to build up a partially molten system. Yet, the details of the different models vary, and therefore results of three numerical codes for two end-member cases are compared.

One model that has been successfully applied for the forward modeling of zircon age spectra is the finite elements (FE) approach of Caricchi et al. (2014, 2016), in which thermal diffusion was solved using an FE approach with periodic sill insertion and passive tracers recording the temperature evolution over time for different portions of the magmatic system. A subsequent version of this model used the finite difference (FD) method to discretize the diffusion equation, whereby the temperature evolution is recorded in each numerical cell that contains magma above the solidus (Weber et al., 2020). These Geneva models track the thermal evolution of a magmatic system assembled by the injection of sills (Fig. 11A), which was previously shown to be chiefly controlled by the thermal state of the crust and the vertical rate of magma accumulation (Annen et al., 2015; Caricchi et al., 2014). Variations of the mode of magmatic injection and geometry of the magmatic system (either randomly in a prescribed volume, or by under-accretion, in which sills are stacked in a downward growth direction) can be modified. These parameters only play a minor role in the long-term thermal evolution of magmatic systems and therefore in the calculated zircon age distributions, but they can produce strongly divergent thermal histories during the early stages of a system (Annen et al., 2006, 2015; Carrigan, 1988; Karakas et al., 2017).

In the Geneva family of models (Fig. 11A), an axisymmetric geometry is assumed, magma is injected at a set temperature (e.g., 1000 °C), and
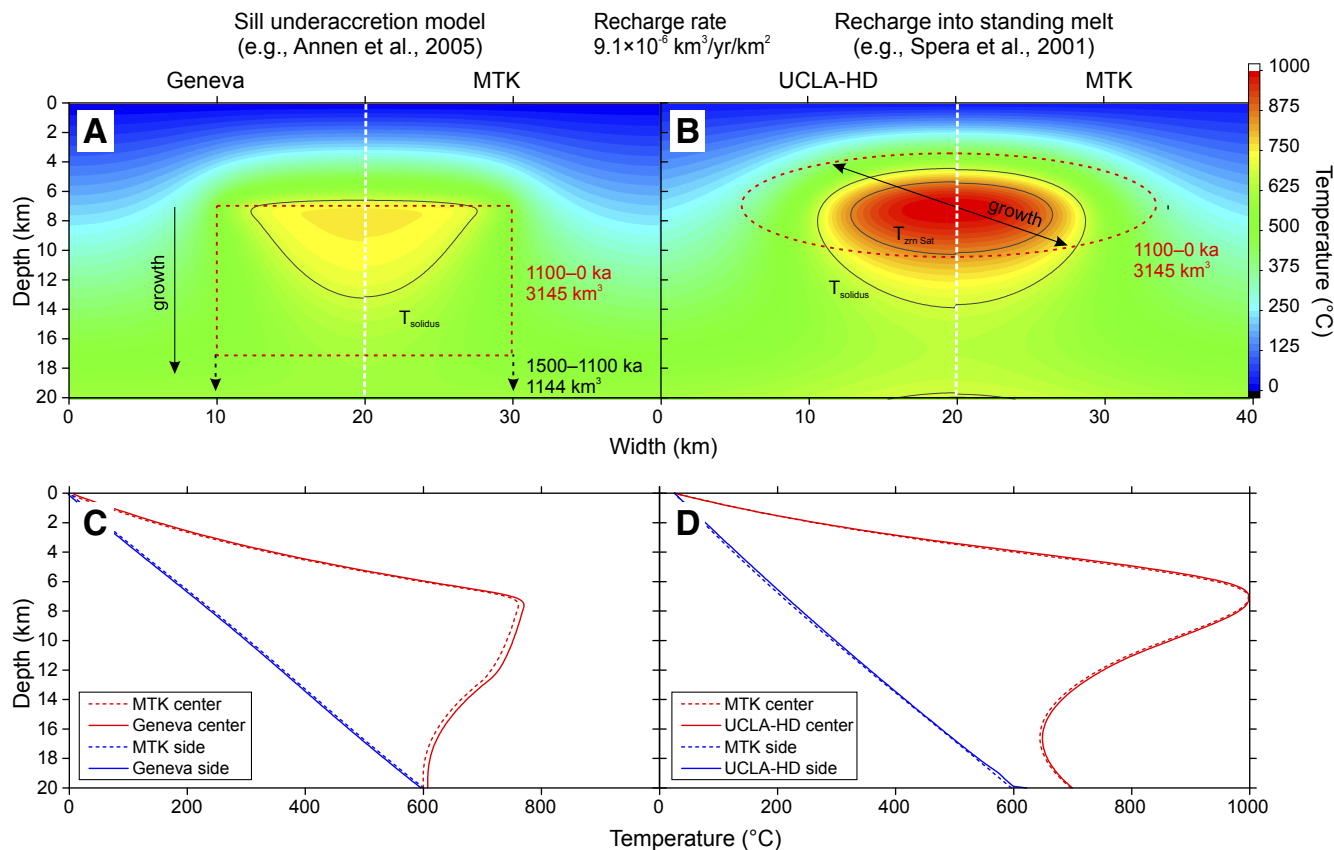
Figure 10. Schematic representation of temporal evolution of temperature and measurable zircon crystallization ages (same prescribed number as in Fig. 9) within a spherical magmatic reservoir growing through input of successive discrete magma pulses. (A) Gray curves show evolution of temperature for magma within each successive injected magma pulse. Black line shows evolution of average temperature within the growing magmatic reservoir. In this case, we consider only the realistic case of exponentially decaying zircon crystallization with decreasing temperature. (B) Schematic distributions of measurable zircon ages resulting from thermal evolution of the reservoir. Note the difference in the distribution if the temperature evolution of each pulse (red) is considered rather than only using the average temperature of the intrusion (black). (C) Schematic distributions of measurable zircon ages for magmatic reservoir portion with temperature sufficiently elevated for the magma to be eruptible. This would be the distribution of zircon age observed in volcanic products at the eruption.

Figure 11. Example of thermal structure of magma emplaced into shallow (depth of intrusion is 7 km) crust in (A) sill under-accretion ("Geneva" model) and (B) recharge into standing melt in the center of an outward-growing ellipsoidal igneous body with horizontal and vertical axes scaling 4:1 (University of California Los Angeles-Heidelberg University [UCLA-HD] model). The magmatic recharge flux in both cases was set to 9.1 × 10⁻⁶ km³/yr/km², with magmatic recharge temperature (1000 °C) and initial geotherm (30 °C/km) identical in both models. Axisymmetric geometry was assumed with fixed bottom-temperature conditions in the Geneva model, whereas the UCLA-HD model kept the bottom thermal flux constant. The intrusion accumulated over 1.5 m.y. in part A, but during an initial (here ~400 k.y.) incubation time (Annen et al., 2015), crustal temperatures were too low to maintain a steady presence of magma, and hence the contribution of zircon that crystallized during incubation is negligible. Thus, the model in part B started later, with the incubation duration in part A being subtracted from the total run duration, so that the resulting zircon age spectra can be directly compared, and with an initial magmatic volume of ~10% of the final intrusive volume being prescribed. Thermal structure at the end of the simulation (corresponding to a zero-age in Fig. 12) is shown, along with the extent of total intrusive volume (red dashed line), and parts of the intrusion above the solidus (black solid line) and the zircon saturation temperature (black dashed line). The left sides of parts A and B show the results of the Geneva UCLA-HD software, whereas the right sides show the results of the MagmaThermoKinematics.jl (MTK) software (see Appendix). (C and D) Temperature profiles are shown at the sides and within the centers of the models based on published studies and newly developed MTK algorithms.

the magma crystallinity (x_f) increases with decreasing temperature (T in °C), as:

$$x_f = 1 - \frac{1}{1 + e^{\theta}}, \qquad (1)$$

where

$$\theta = \frac{(800 - T)}{23}. \qquad (2)$$

Alternatively, the relation between T and x_f was estimated from a fourth and fifth order polynomial fit to the experimental melt fraction temperature curves of Blatter and Carmichael (2001) and Marxer and Ulmer (2019). The time-temperature (t-T) trajectories of the system are then derived from a large number (e.g., 1000) of passive tracers sampling temperature at constant time intervals between the onset and the end of magmatic injections. Each tracer can produce an arbitrary number of measurable ages (e.g., 100), and the rate of zircon crystallization decreases with decreasing temperature following the derivative of Equation 3 for T (Tierney et al., 2016):

$$F_{zr} = \left\{1.62 - 1.8 \cdot 10^4 \, e^{-\frac{10^4}{T}}\right\} \cdot zr_m, \qquad (3)$$

where the cumulative fraction of zircon (F_{zr}) for each unit of magma increases with decreasing T, and zr_m is the maximum fraction of zircon crystallizing between zircon saturation (T_{zr}) and the solidus temperature (T_{sol}). At the time when the zircon population is sampled (e.g., in a volcanic eruption), only tracers with a temperature higher than a minimum temperature (T_{min}) are considered. T_{min} can represent either the minimum temperature at which magma (and zircon therein) can erupt, or the temperature of the interstitial melt extracted (together with zircon) to feed a volcanic eruption. The tracer that spends the longest period within the temperature interval of zircon saturation provides the maximum possible duration of continuous zircon crystallization. Once this is determined, all measurable ages between the

oldest age and the time of eruption are summed as schematically shown in Figure 10.

The second type of model (UCLA-HD; Friedrichs et al., 2021; Tierney et al., 2016) starts with a two-dimensional grid of 0.1 × 0.1 km cells over a 20 × 60 km (width × depth) rectangle that represents a mid–upper crustal block. Parameters for modeling the thermal and compositional evolution of magma and its surroundings within this grid are based on equations for recharge-assimilation–fractional crystallization (RAFC; Spera and Bohrson, 2001). Geometrically, the UCLA-HD model differs from the Geneva models in that instead of vertically stacking sills from a prescribed depth and typically displacing the crustal rocks downward (e.g., Weber et al., 2020), magmatic injection always occurs in the center of an ellipsoidal volume of magma, i.e., the hottest and therefore likely most long-lived standing volume of magma in the intrusive body (Fig. 11B). Upon growth due to periodic magmatic recharge, the body maintains its originally defined aspect ratio. The thermal evolution of individual cells is monitored throughout the simulation as they migrate away from the center of magmatic recharge and are translated into a pseudo-3–D distribution assuming rotational symmetry around the vertical central axis of the magmatic body in the center of the grid.

The crystal fraction, x_f, is calculated somewhat differently from that of the Geneva model (Caricchi et al., 2014, 2016) by using the following relationship:

$$x_f = \left[\left(T_{liq} - T \right) / \left(T_{liq} - T_{sol} \right) \right]^2, \qquad (4)$$

where T_{liq} and T_{sol} are the liquidus and solidus temperatures of the recharge magma, respectively. The temperature of magmatic recharge is selected based on reasonable geological constraints (e.g., based on thermometry of co-erupted mafic rocks; Friedrichs et al., 2021). At each time-step during the model run, the temperature change of each cell is monitored: For each cell undergoing cooling within the saturation range (e.g., 800–700 °C), the

fraction of zircon growth is then calculated using Equation 3. This results in a time-resolved zircon growth curve for each cell, and each curve is then summed at the time of eruption. Only cells that are above 700 °C (super-solidus) are considered and weighted according to their relative volumes when translating the 2-D grid into 3-D. These zircon growth curves distinguish between core (e.g., at 20% of each curve) or rim ages (e.g., at 80%; Friedrichs et al., 2021). An average total zircon age can also be obtained from the integration of the entire zircon growth curve.

A limitation of existing numerical modeling studies that simulate the thermal evolution of magmatic systems is that the source code is typically not readily accessible in publications, and the assumptions behind the models often vary according to a particular geological setting, which makes comparison of the different studies difficult. Moreover, numerical implementation details, such as how to deal with nonlinearities, are beyond the limits of typical publications, which limits reproducing results. Therefore, we developed a new Julia package to simulate the thermal evolution of magmatic systems (MagmaThermoKinematics.jl, or briefly MTK). The new package is open source and works in 2-D, 2-D axisymmetric, and 3-D geometries. It utilizes modern hardware such as graphics processing units (GPUs) and multicore processors and provides a simple yet extendable way to change material parameters (see the Appendix for a detailed description). Several dike injection algorithms are implemented, including one that employs an analytical solution to insert coin-shaped cracks into an elastic half-space, as well as central injection and sill under-accretion. Tracers are injected within newly added dikes and record the subsequent thermal evolution from which zircon age distribution can be calculated. We have benchmarked this third modeling approach versus the two end-member scenarios shown in Fig. 11, which demonstrate that differences in the thermal structure are generally <5 °C at the end of the simulation (see Fig. S1 in the Supplemental Material[1]).

Overall, both model geometries define plausible end-members of multi-cyclic intrusions, where the Geneva sill geometry leads to initially more rapid heat dissipation (especially when the depth of sill emplacement is random, rather than vertically stacked) compared to the UCLA-HD model, where the ellipsoid has a smaller surface-to-volume ratio than a thin cylindrical sill, and recharge always occurs in the hottest part of the system. Crustal thermal conditions prior to intrusion are defined in both models as constant mantle and surface heat flow. Country-rock partial melting and assimilation (Spera and Bohrson, 2001), as well as radioactive heating, are irrelevant for comparatively brief model-run durations and the shallow depth of sub-volcanic igneous bodies and their low country-rock temperatures.

To understand how differences in the choice of material parameters and boundary conditions affect the thermal structure, we systematically varied many of the parameters for the two scenarios. Results show that the central intrusion setup is very robust with respect to variations in the material parameters, and that the sill under-accretion case has larger variations (Fig. S1; see footnote 1). This difference is mostly likely caused by the sill under-accretion case not having reached steady-state yet, even over 1.5 m.y. run durations, whereas this is the case for the central intrusion case.

3.3 Describing Calculated and Measured Age Distributions

In principle, knowing the thermal conditions in an intrusion at any time allows calculation of the number of possible zircon crystallization ages potentially available for measurement. The calculated number of measurable ages can then be converted into a PDP (normal or cumulative) for comparison with the distribution of measured ages (Fig. 12). Alternatively, a simple parameter, such as the age difference (Δt) between stated percentiles of the modeled zircon age distribution, can be used

---

[1]Supplemental Material. Figure S1. Results of simulations in which we systematically changed a single model parameter, starting from the reference simulations shown in Figure 11. Please visit **https://doi.org/10.1130/GEOS.S.22898453** to access the supplemental material, and contact editing@geosociety.org with any questions.
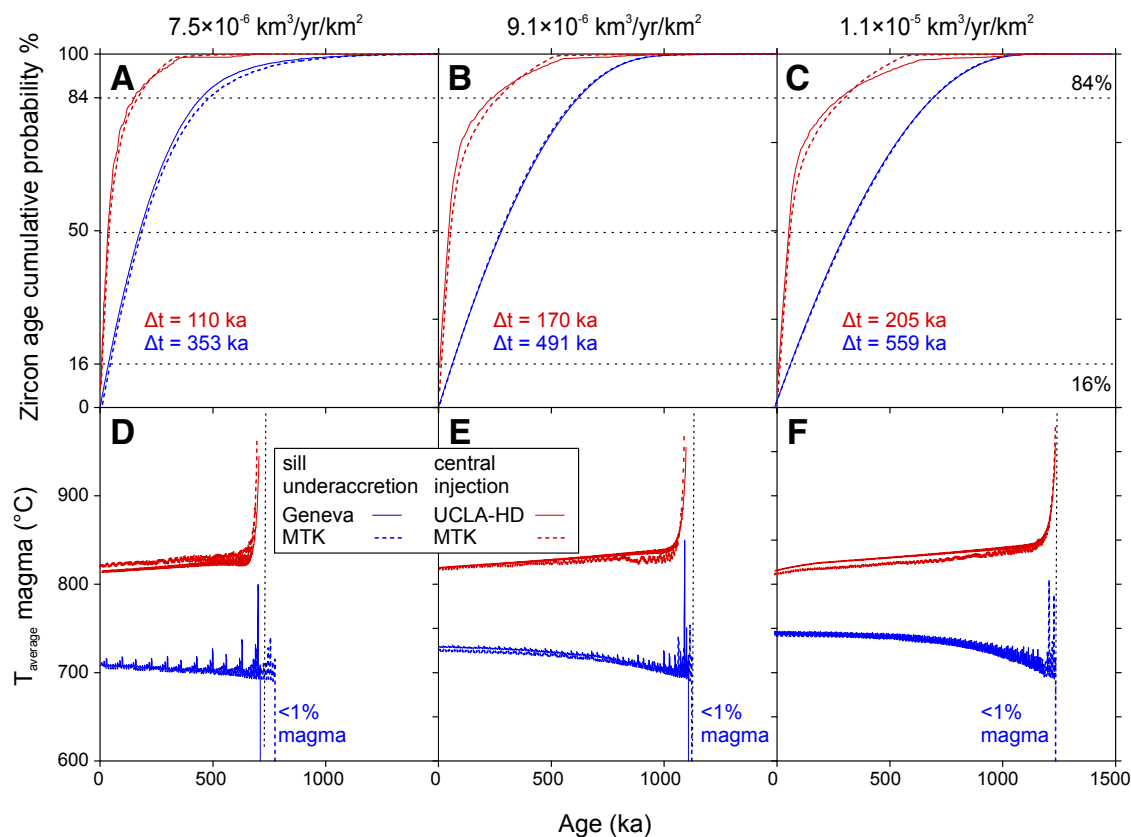
Figure 12. Comparison of cumulative probability density plots (PDPs) of (A–C) zircon ages and (D–F) average magmatic temperature (all domains in the igneous body with temperatures >700 °C) modeled for a magmatic body generated by frequent magmatic recharge in sill geometry (blue lines; Geneva model), and injection into the center of an ellipsoid (red lines; University of California Los Angeles-Heidelberg University [UCLA-HD] model) with recharge fluxes of 7.5×10^{-6}, 9.1×10^{-6}, and 1.1×10^{-5} km^3/yr/km^2. Runtime for the Geneva models was always 1.5 m.y.; corresponding durations for the UCLA-HD models were shortened to (A–C) 0.7 m.y., 1.1 m.y., and 1.3 m.y., respectively, to exclude the incubation time required to establish continuous melt presence in the Geneva models (see Fig. 11). Initial magmatic volumes in the UCLA-HD models were 10% of the final volumes, which are 1641 km^3, 3145 km^3, and 6100 km^3 in parts A, B, and C, respectively. Results from MagmaThermoKinematics.jl (MTK) models using both geometries and methods to compute zircon ages yielded equivalent results, which underscores the robustness of the different numerical approaches. Due to different geometries, Δt and final average temperatures differ, but the shapes of model zircon age distributions are generally similar.

for comparison (e.g., using the 16–84 percentile difference, corresponding to ± 1 s.d., although the resulting distributions in both types of models are strongly skewed toward younger ages; Fig. 12). In the model-scenario examples (Fig. 12), Δt systematically increases with the duration of continuous melt presence and recharge rate. The input parameters of the model that best match the measured distribution of zircon ages can then provide a quantitative estimate of processes operating in a long-lived crustal intrusive body, such as the rate of magma recharge. However, this would be true only if dating could be performed in each zone for a large number of zircon crystals. Instead, actual data sets are necessarily limited in number and resolution, and it is thus important to consider how

to compare the modeled and natural distribution of zircon ages measured with ID-TIMS or high spatial resolution techniques.

3.4 Measurement Bias in Age Distributions

Before discussing applications of these models, we first focus on the analysis of zircon collected in plutons and discuss the modifications to apply to the modeling when dealing with zircon from volcanic products. The properties of a natural zircon age distribution are captured by common analytical techniques such as ID-TIMS, LA-ICP-MS, and SIMS, which afford age resolution to different degrees depending on their required sampling volumes

(Table 1). To demonstrate the potential differences between these types of data in an idealized case, we simulate a pool of 200 zircon crystals (assumed to be spherical for simplicity) spanning an age range of 3 m.y., with radii between 50 μm and 100 μm, and with the thickness of the different zones selected randomly but arranged to decrease from the crystal center toward the rim (a selection is shown in Fig. 13A). The U content of the different zones and the variation of the zircon zone thickness from core to rim affect the distributions of ages obtained from whole zircon versus high spatial resolution techniques (Curry et al., 2021). In this simulation, each zircon comprises 2–10 zones of decreasing age from core to rim and only zircons with 10 zones have a core with the oldest age (i.e., 3 Ma). During the
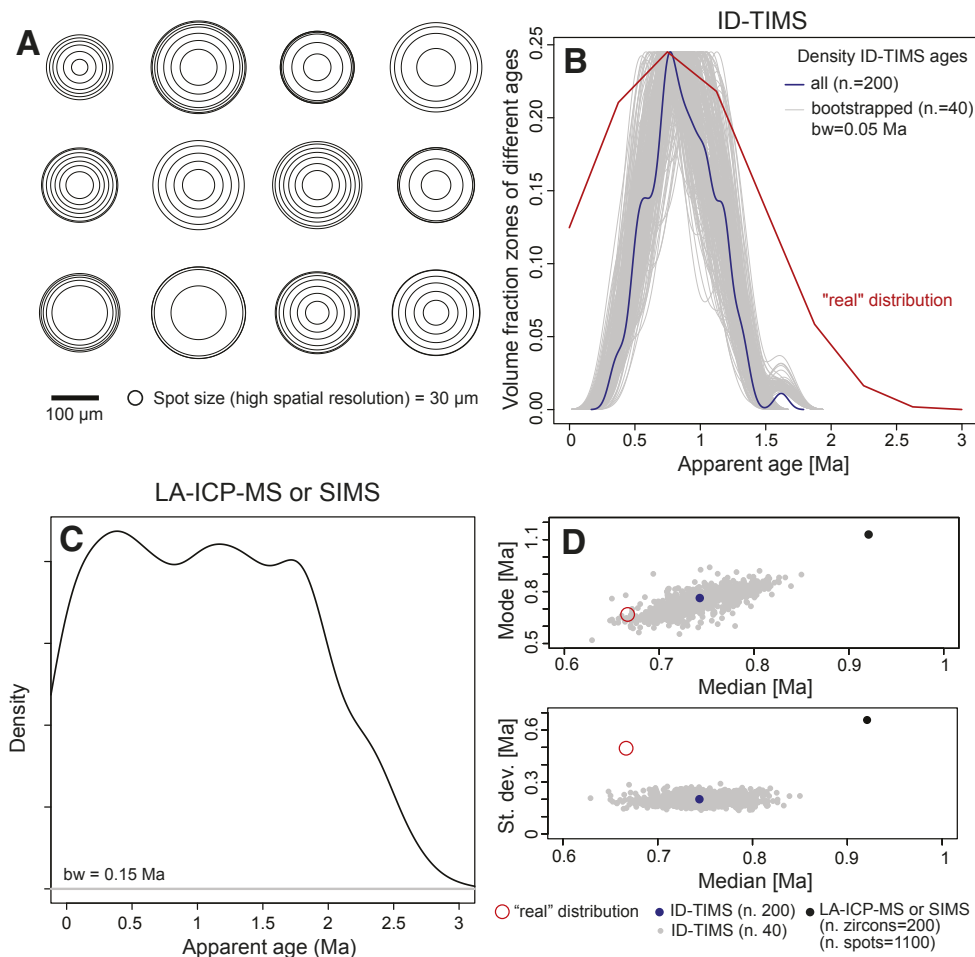
Figure 13. (A) Simulated, randomly assigned zircon age zonations, and resulting age distributions for methods sampling different volumes of zircon (B: isotope dilution–thermal ionization mass spectrometry [ID-TIMS], C: laser ablation–inductively coupled plasma–mass spectrometry [LA-ICP-MS] or secondary ionization mass spectrometry [SIMS]; bw = sampling bandwidth). Part D plots median age versus mode and standard deviation for the "real" distribution (red open circle) and different samplings using multiple spots on various types of crystal.

would be obtained using ID-TIMS is significantly shorter than the "real" duration of the magmatic event during which zircon was crystallizing (Fig. 13; Glazner and Sadler, 2016). However, it is interesting that the median and mode for the calculated ID-TIMS analysis are relatively close to the real values, whereas the standard deviation is generally underestimated by the subsamples (Fig. 13D). Thus, for ID-TIMS age determinations, mode and median provide relatively reliable metrics for comparison of modeling results, whereas the true standard deviation of ages is underpredicted. This test implies that using ID-TIMS ages in combination with the model proposed by Caricchi et al. (2014, 2016) is appropriate and produces relatively good estimates for the rate of magmatic input into the system but underestimates the volume of the system.

Using the same simulated population of zircon crystals, we calculated the distribution of ages that would be measured by placing 1100 analysis spots of a high spatial resolution technique (LA-ICP-MS or SIMS) with a beam diameter of 30 µm (Fig. 13A). We assume that crystals are analyzed in cross-sectioned mid planes, disregarding mixing of crystal domains at different depths for simplicity. High spatial resolution analyses better capture the total duration of zircon crystallization, but because of lateral mixing of growth domains, they provide biased estimates for the mode and median of the actual distribution of zircon ages (Fig. 13D). Therefore, the comparison between the calculated distribution of zircon ages and measurements performed using high spatial resolution techniques should focus on the total spread of zircon ages (e.g., as described by the standard deviation) rather than on the mean or median. The exceptions are analyses of unsectioned crystals acquired in depth-profiling mode (e.g., Schmitt and Vazquez, 2017), in which the ion beam ideally samples individual growth domains with minimal mixing as the depth resolution of the ion beam (<1 µm) is small relative to the dimensions of the growth zones. Surface analysis of individual and unsectioned zircon crystals also allows age determination of the last growth episodes largely without mixing different growth zones, and thus not only the total spread can be modeled, but also

prescribed 3 m.y. of magmatic history that zircon could potentially record, the mass fraction of zircon crystallized increases as the amount of magma capable of crystallizing zircon grows, but then drops toward the end of the interval to mimic the waning stages of the magma system, consistent with the expected zircon age distributions introduced in

section 3.3 (Fig. 13B). We then use this simulated zircon production curve to calculate the distribution of zircon ages that would be obtained by performing ID-TIMS analyses by summing the product of the mass fraction of each sector and the respective age of the sector (Fig. 13B). Not surprisingly, this calculation shows that the range of zircon ages that

the shape of the probability density function (i.e., the relative proportions of newly crystallized zircon relative to antecrystic grains).

3.5 Comparison of Different Thermochemical Models for Zircon Crystallization in Magmatic Systems Evolving through Recharge

Although direct comparability between the currently applied models as summarized in section 3.2 is complicated by the fundamental differences in how they are conceptualized and coded, we can demonstrate general similarities between the predicted thermal histories for magmatic systems open for recharge over typical lifetimes of volcanic systems (e.g., 1–1.5 m.y.; Weber et al., 2020). To mitigate model-dependent bias, we calculated zircon crystallization ages for both models using identical boundary conditions. For this, conditions typical of a long-lived arc volcano were selected, which include a normal initial geothermal gradient of 30 °C and a magma recharge temperature of 1000 °C (Weber et al., 2020). Furthermore, both types of models were set up to produce the same total magmatic volumes with an approximately identical depth range of the accumulated intrusion after the end of each run (Fig. 12). A corollary of the cylindrical sill geometry with downward displacement is that the magma always comes into contact with comparatively cold crust, and the magma will thus be more affected by rapid initial cooling than the outward growing ellipsoid, as earlier intruded and hot magma/rock shields the interior of the ellipsoid from heat loss to cold country rocks. To compensate for a protracted initial incubation time in the Geneva models during which zircon productivity is negligible, the run duration of the UCLA-HD models was shortened to only match the zircon-producing duration of the Geneva models (as defined by the presence of ~1% of final magmatic volume). The volume of the initial intrusion that becomes inflated by continuous recharge (in pulses every 5000 years) was prescribed as ~10% of the final intrusive volume in the UCLA-HD model, and the aspect ratio of the ellipsoid was held constant (horizontal:vertical axes = 4:1). As a result,

the average magmatic temperatures are always lower for the Geneva model than for the UCLA-HD model, with temperatures gradually increasing and decreasing with the run duration, respectively (Fig. 12). This is expectedly matched by the longer duration of zircon crystallization (measured as the difference between the 16th and 84th percentile in the cumulative zircon age distribution) in the overall cooler Geneva models relative to the hotter UCLA-HD models at the modeled magmatic recharge rates of 7.5×10^{-6} to 1.1×10^{-5} km³/yr/km² (Fig. 12). Despite these differences, the overall shape of the cumulative probability distribution of expected zircon ages is similar, which implies that under the selected conditions, sampling of younger zircon is more likely than sampling of older crystals due to progressive growth of the zircon-saturated thermal layer.

3.6 Implications of Zircon Age Spectra Modeling

Despite conceptual and computational differences in the setup of thermochemical models for zircon crystallization in evolved magmatic systems fed and maintained by a repetitive influx of more primitive magma, they provide broadly similar results. This can yield unique quantitative constraints on long-term magmatic fluxes and magmatic crustal accretion in a specific tectonic environment. In contrast to geophysical observations that monitor present-day conditions, modeling the thermal evolution of magmatic chambers as tracked by their zircon inventory can reveal long-term variations in magmatic input in long-lived systems, and it can also be applied to fossil magmatic systems in the form of plutons.

One important insight gained from the modeling of zircon age spectra is that substantial intrusive volumes accumulate under arc volcanoes. Hence, intrusive to extrusive ratios determined by this method for volcanic arcs range from 25:1 to 50:1 for Nevado de Toluca, a stratocone in the Trans-Mexican Volcanic Belt (Weber et al., 2020), to 75:1 for lava domes in the Altiplano-Puna region, which erupted after an ignimbrite flare-up episode

(Tierney et al., 2016). These exemplary estimates significantly exceed the commonly inferred intrusive to extrusive ratio of 10:1 (Crisp, 1984). The intrusive to extrusive ratio also changes as a function of time and tends to decrease in thermally mature volcanic systems (Giordano and Caricchi, 2022, and references therein).

Zircon growth models also quantitatively predict volumes of eruptible magma in the subsurface that can be directly compared with those estimated from other petrological constraints (e.g., Weber et al., 2020; Friedrichs et al., 2021) or geophysical observables (e.g., Lukács et al., 2021). To illustrate how zircon age spectra and their quantitative modeling can reveal fundamental differences between the underlying magma systems, we compare data from four volcanoes recently studied (Fig. 14). Here, this can only be accomplished in an abridged form, and we refer to the cited publications for more detail (Weber et al., 2020; Friedrichs et al., 2021; Lukács et al., 2021).

One key outcome of these studies is that potentially eruptible volumes of magma can be significant in systems that are currently dormant, or even considered extinct by conventional standards, but also that volumes of potentially eruptible magma vary significantly in different systems. This is important in assessing mid- to long-term hazards from volcanoes (e.g., Lukács et al., 2021; Weber et al., 2020). The estimates for the total amount of eruptible magma (at <50% crystal content) derived from modeling zircon age spectra are comparatively small (albeit non-negligible) for the Ciomadul dome field of Romania at ~5–10 km³ (Lukács et al., 2021), whereas for Nevado de Toluca, the total amount of eruptible magma is about one order of magnitude larger (Figs. 14A and 14B; Weber et al., 2020). This agrees with the overall differences in cumulative eruptive volumes (8–10 km³ for Ciomadul versus ~60 km³ for Nevado de Toluca), and eruptive frequency (e.g., last major eruption at ca. 30 ka for Ciomadul versus ca. 14 ka for Nevado de Toluca).

Zircon age spectra can also indicate variations in magmatic recharge fluxes over time (Friedrichs et al., 2021; Angeles-De La Torre et al., 2023). This is the case for two adjacent stratovolcanoes in Central Anatolia (Mt. Hasan and Mt. Erciyes) that
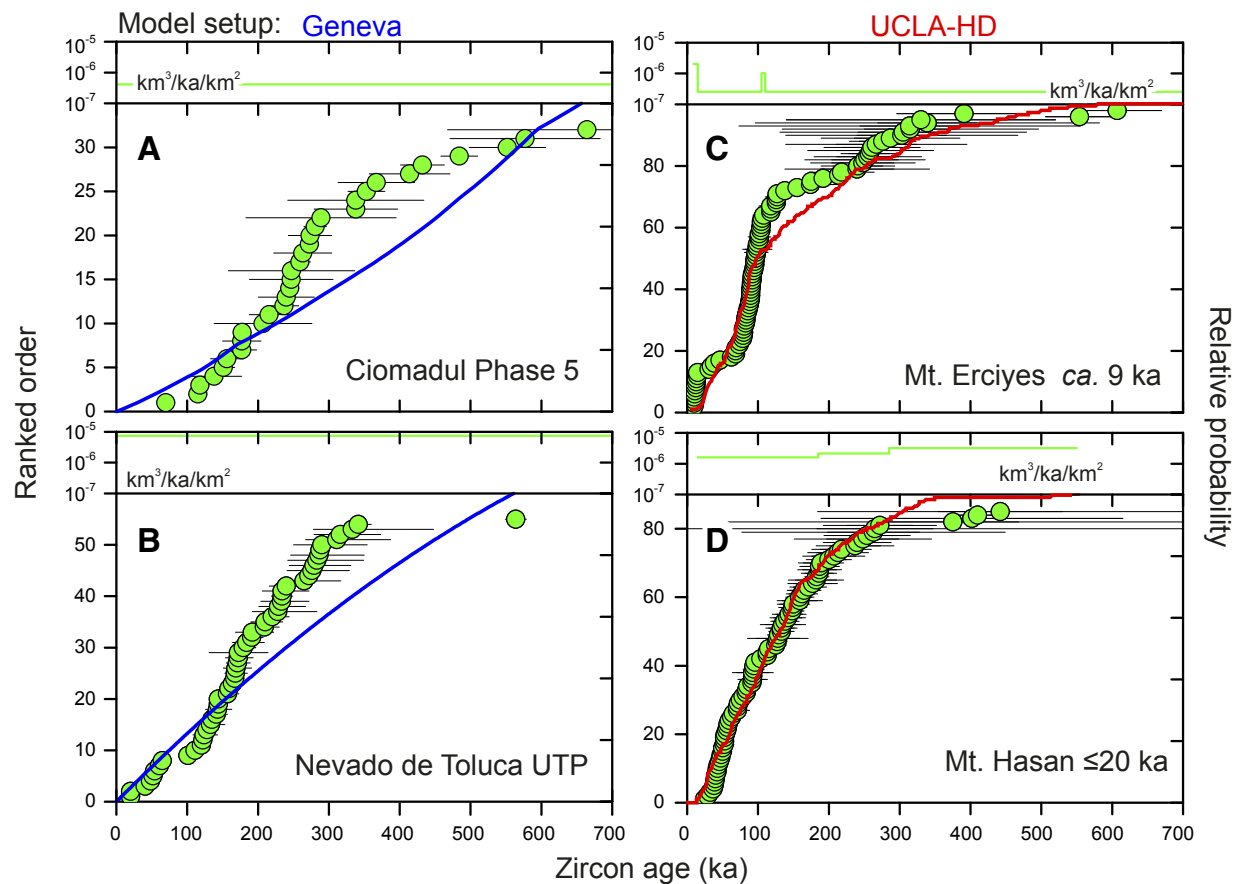
Schmitt et al. | Zircon age spectra

Figure 14. Zircon age spectra as ranked order plots plotted with model zircon age curves as cumulative probability density plots based on different intrusion geometries in the (A, B) Geneva and (C, D) University of California Los Angeles-Heidelberg University (UCLA-HD) models. (A) Ciomadul dome complex representing a small, dormant system, for which U-Pb zircon interior ages from the youngest eruptions (Phase 5 is between ca. 50 ka and 30 ka; Lukács et al., 2021) are plotted; (B) Nevado de Toluca, a large stratocone that is currently dormant but has experienced multiple large-volume explosive eruptions in the late Pleistocene, with U-Th and U-Pb interior analyses shown for the 12.5 ka Upper Toluca Pumice (UTP) eruption (Weber et al., 2020); (C) Mt. Hasan; and (D) Mt. Erciyes, both strato-volcanoes in central Anatolia (Friedrichs et al., 2021); data sets comprise U-Th and U-Pb interior ages with xenocrystic zircons from Mt. Erciyes (with the youngest ages down to ca. 2 Ma) omitted. Mt. Hasan has an eruptive history of steady andesitic lava flow effusion with a ca. 5–15 k.y. recurrence interval in the late Pleistocene, whereas Mt. Erciyes experienced its penultimate eruptions at ca. 105–85 ka followed by an eruptive hiatus before an early Holocene reawakening, when a series of peripheral rhyolitic domes erupted (Friedrichs et al., 2021, and references therein); only data from the most recent eruptions of both volcanoes are plotted. Curves above the ranked order plots show (A, B) constant or (C, D) variable recharge rates used in different models. Models in A and B were run between 1.5 Ma and 2 Ma and 0 ka (eruption age), with an incubation time during which no zircon was produced (see text); eruption ages were subtracted from measured zircon ages. Model curves in parts C and D were calculated from 800 ka (Mt. Erciyes) and 550 ka (Mt. Hasan) to the respective eruption ages; measured ages are shown. For ease of comparison, all areal rates were calculated here for a magmatic system circumscribed with a 10 km radius; for specific areal extent of volcanic edifices, see original studies.

show different styles of continuous versus pulsed recharge throughout the late Pleistocene (Figs. 14C and 14D; Friedrichs et al., 2021). One important aspect of the study by Friedrichs et al. (2021) is that zircon crystals were separated and analyzed following identical protocols for samples from both volcanoes so that the observed differences in the age spectra are robust. Moreover, different patterns in long-term recharge rates, steady and frequent for Mt. Hasan versus fluctuating and infrequent for Mt. Erciyes, correlate with the eruptive frequency and type for each volcano, which are characterized by frequently recurring lava flows of

intermediate (andesitic) composition for Mt. Hasan and initially highly explosive eruption bursts of evolved (rhyolitic) magmas from multiple vents for Mt. Erciyes (Friedrichs et al., 2021). Zircon age spectra modeling suggests that the active magmatic system underneath Mt. Hasan is larger and more frequently rejuvenated by mafic magmatic input, whereas that of Mt. Erciyes has shrunk to contain mostly residual evolved melts in what may represent the waning stages of its magmatic system, despite the overall larger volcanic edifice volume compared to that of Mt. Hasan (Friedrichs et al., 2021).

As these examples illustrate, interpretation of zircon age spectra should ideally integrate as much geological information as possible, including the eruptive pre-history of a volcanic system. The onset of magmatic input into the system is especially important for refining estimates of the rates of magmatic input at depth. This is because the dominant factor controlling the thermal evolution of the magmatic system is the total amount of sensible heat added into the crust, which is the product of the rate of magmatic input and time. The onset of magmatic input can either be obtained from the oldest (non-xenocrystic) zircon or by dating

the first eruption of a volcanic system, e.g., with $^{40}Ar/^{39}Ar$ or (U-Th)/He chronometers. On one hand, both approaches will likely underestimate the duration of magmatic input into the plumbing system, as zircon only starts crystallizing once sufficiently evolved melts are generated, and products of older eruptions may be covered or destroyed. On the other hand, it is sometimes difficult to distinguish between antecrysts and xenocrysts (Miller et al., 2007), which may lead to an overestimation of the onset of magmatism.

The thermal models presented in section 3.2 illustrate how for similar zircon age distributions, the average temperature can change significantly when different geometries of magmatic input into the plumbing system are considered (Figs. 12D–12F). Such differences should be reflected in different abundances and temporal trends in the chemistry of volcanic products, as well as the trace-element characteristics of zircon. Hence, knowing the temporal and chemical evolution of volcanic products and zircon from eruptions spanning the widest possible time interval provides additional constraints for identifying the most appropriate thermal model. This, in turn, allows the retrieval of more accurate and precise estimates of the average rates of magmatic input into the volcanic plumbing system. The same approach could be applied to exposed crustal sections by focusing on plutons spanning the widest possible range of emplacement ages. Studies that complemented zircon age spectra with thermochemical indicators, such as trace element data, have demonstrated this potential (e.g., Ti-in-zircon; Samperton et al., 2017; Kent and Cooper, 2018; Weber et al., 2020; Friedrichs et al., 2021).

Models such as those shown in Figures 11 and 12 indicate that protracted zircon crystallization in a long-lived system open for recharge results in a distribution of zircon ages in volcanic rocks that differs significantly from that expected from zircon saturation in a magmatic volume that (unrealistically) cools without any internal thermal gradients. Zircon age spectra, successfully modeled in terms of open-system magmatic recharge, thus may have little in common with the simple exponential decrease in zircon production predicted from zircon

saturation models for a single batch of melt undergoing monotonic cooling (e.g., Harrison et al., 2007). The models described in section 3.2 suggest zircon distributions for long-lived silicic magma systems with younger zircon predominating over older zircon, the opposite of the distribution expected for cooling of a single-magma batch (Figs. 9 and 10). This implies that it is not straightforward to prescribe an a priori age distribution to zircon age spectra to extract eruption ages from zircon data. Thus, extrapolating from zircon ages to a precise eruption age (e.g., Keller et al., 2018) requires firm knowledge of the pre-eruptive zircon crystallization history of a particular magmatic system. Because zircon ages track the pre-eruptive accumulation of magma, they are an important complement to eruption ages for unraveling potential leads and lags regarding climatic variability (e.g., sea-level changes and glaciation–deglaciation) and associated lithospheric stresses that may influence the productivity of magma, recharge fluxes, and eruptive frequency (e.g., Satow et al., 2021).

3.7 Future Developments for a Better Interpretation of Zircon Age Spectra

To further advance zircon as a magmatic thermochronometer, improvements in analytical methodology and more realistic models for zircon crystallization, residence, and mobilization in magmas are required. Because zircon age spectra based on a few analyses may not reliably represent the underlying distribution, large-n data sets ($n > 100$) will potentially provide additional information, in line with the approach advocated for state-of-the-art detrital zircon studies (Pullen et al., 2014). Moreover, there are analytical limitations in resolving the true duration of zircon crystallization (Table 1). To further utilize the potential to reconstruct thermal histories from individual zircon crystals, improved spatial resolution and precision are essential. Zircon trace-element geochemistry also furnishes complementary information such as temperature (Ti-in-zircon) and melt evolution (e.g., indices for differentiation such as Zr/Hf and Eu/Eu*, as well as for crustal assimilation such as

$\delta^{18}O$ and ϵHf) that can be used alongside and in support of the age data. Lastly, the understanding of the significance of zircon ages is limited by the fact that, in most studies, textural relationships of zircon to other mineral phases are unknown because zircon is extracted from its matrix by physical and chemical methods. Therefore, it remains ambiguous whether an individual zircon crystal stopped crystallizing because it became entombed in major minerals and therefore was shielded from the melt, or because of subsolidus cooling and complete solidification of the magma.

Although zircon saturation is well constrained, zircon can crystallize before whole-sale saturation is reached when melt composition and Zr abundance become locally conducive for zircon crystallization, e.g., when zircon crystallizes next to fast-crystallizing oxides (Bacon, 1989). A related critical aspect is that evolved (per-)alkaline system compositions currently defy modeling zircon crystallization because experimental constraints for zircon saturation in such melts are scarce (cf. Gervasoni et al., 2016). Empirically, zircon crystallizes late in such systems due to the high solubility of Zr and Hf in alkaline melts (Linnen and Keppler, 2002), but then crystallization from supersaturated, volatile-rich, and low-viscosity melts can produce large amounts of zircon, often much larger in grain size than those that crystallized from metaluminous or peraluminous melts. The processes of zircon saturation and growth in such melts, along with the formation of hydrothermal zircon (e.g., Troch et al., 2018), should receive more attention in the future.

3.8 Unifying Reactive Two-Phase Thermo-Mechanical Models of Magma Transfer

The thermal models presented in section 3.2 are severely restricted in realistically describing mixtures between crystals and melt where relative proportions of solids and liquids are expected to fluctuate spatially and temporally over the lifetime of a magma system. Re-mobilization of crystal-rich marginal domains or convective overturn in a magma prior to volcanic eruptions are disregarded in these models, although both processes are likely

common in nature. Rounded and partially melted plutonic enclaves are frequent ingredients of volcanic deposits, which suggests that the reheating of largely solidified magmatic crusts can liberate zircon from otherwise non-eruptible domains of a magmatic system (e.g., Schmitt et al., 2010). Furthermore, massive recharge events are expected to cause remobilization, stirring, and homogenization over large distances in a long-lived crystal mush (e.g., Bachmann and Bergantz, 2006; Huber et al., 2009). This seems to be a prerequisite for indistinguishable zircon age spectra at the hand-specimen scale for the same eruption despite these crystals originating in different parts of a magmatic reservoir and thus recording different thermal histories (e.g., Pamukçu et al., 2022). The frequency and intensity of these remobilization and overturning events in long-lived magmatic systems are empirically poorly constrained.

Creating a petrologically grounded thermo-mechanical model applicable to magmatic systems is one of the biggest challenges of geodynamic modeling. Indeed, such a model has to integrate: (1) complex elasto-viscoplastic rheologies for the deforming host rock; (2) several modes of magmatic transport/segregation, including mass convection, pervasive flow within an interconnected solid network (low melt/rock ratio), settling of crystals within a magmatic body (high melt/rock ratio), and diking through the host-rock (high melt/rock ratio); (3) end-member cases where either fully solidified rock or fully liquid magma is present; (4) extremely large viscosity difference between magma and solid host; (5) thermodynamically consistent phase stabilities and transitions, involving reaction kinetics, volume change, and thermal stress; and (6) the coupling of tectono-magmatic processes occurring over a wide range of temporal and spatial scales in a self-consistent and numerically stable way.

State-of-the-art approaches are currently divided into three main categories that tackle these problems from different angles. The first category aims to better couple thermo-mechanical deformation with two-phase flow while disregarding or simplifying phase reactions (e.g., Keller et al., 2013, 2017; Keller and Katz, 2016; Turner et al., 2017; Rummel et al., 2020; Keller and Suckale, 2019; Katz et al., 2022).

Although significant breakthroughs have been achieved during the last decade, to date there are no elasto-plastic thermo-mechanical models that are able to account for volume change and phase reactions simultaneously. Instead, the second category has focused on coupling two-phase flow models with phase reaction while disregarding thermo-mechanical deformation (e.g., Jackson et al., 2003, 2005; Annen et al., 2006; Bouilhol et al., 2011; Solano et al., 2012; Jackson et al., 2018; Riel et al., 2019). Here, several 1-D models of reactive two-phase flow have been successfully conducted, but only a limited number of 2-D applications have investigated the formation of a reactive melt-filled network (e.g., Bouilhol et al., 2011), and all ignore the role of elasto-plastic thermo-mechanical deformation of the host-rock, including diking. Moreover, the coupling with phase reactions is mainly achieved using simplified parameterizations (e.g., Jackson et al., 2003, 2005, 2018; Solano et al., 2012), which provides useful insights into the overall model behavior but makes it difficult to directly compare the simulations with geochemical data. The third category aims to better understand the relationship between magmatic chamber recharge and eruption. Using a 0-D modeling approach, these models consider up to three phases (solid, liquid, and gas), visco-elasto-plastic rheology of the surrounding crust, parameterized thermodynamically consistent phase changes within the magma chamber, as well as pressure variations related to recharge and eruptions events (e.g., Degruyter and Huber, 2014; Townsend et al., 2019; Townsend and Huber, 2020; Townsend, 2022; Liao et al., 2021). Although the latter category allows scaling relationships to be drawn based on eruption frequency and size (e.g., Degruyter and Huber, 2014; Townsend et al., 2019; Townsend and Huber, 2020; Townsend, 2022), it falls short of describing the internal dynamics of a magmatic chamber and has yet to be applied to higher spatial dimensions.

Melt segregation within magmatic chambers and cycling between magmatic recharge and extraction in and out of a magmatic reservoir imply that compositions of crystals and melts are constantly evolving. Hence, the use of phase equilibrium parameterization or look-up-tables of fixed bulk-rock

composition cannot predict the chemical evolution of the magmatic chamber. Alternative methods, such as a pre-computed petrological database covering the expected compositional space (Rummel et al., 2020), or direct coupling with a Gibbs free energy minimizer (Riel et al., 2019, 2022) is a step forward. The coupling of a physical model of melt extraction and crystal accumulation in a magma chamber to a petrological database (Rummel et al., 2020) or a Gibbs energy minimizer (e.g., Riel et al., 2019), while challenging on its own, can allow the mechanical and chemical evolution of a magmatic reservoir to be modeled. With adequate zircon saturation models or a thermodynamic database that includes Zr (Kelsey and Powell, 2011), the growth and resorption of zircon can be readily predicted. However, the sluggish dissolution kinetics of zircon in silicate melts (e.g., Watson, 1996; Bindeman and Melnik, 2016) also play an essential role in controlling the available Zr pool for zircon crystallization. Therefore, the coupling of thermo-mechanical models for magmatic chamber dynamics and petrological reactions also needs to account for non-equilibrium thermodynamics. A possible solution could be to use stable phase equilibrium prediction as a directional step (e.g., Lasaga, 1986), while the length of that step, which corresponds to the reaction kinetics, could be constrained by experimental melting studies (e.g., Hou et al., 2020).

■ 4 CONCLUDING REMARKS

Zircon, although a tiny and seemingly negligible component in rocks, is nonetheless an essential probe into magmatic systems concealed at depth. It is not only a time capsule, but also a faithful recorder of the thermal and chemical conditions in magmas. For these reasons, zircon has become indispensable for studying differentiation, longevity, and pre-eruptive priming of magmatic systems, where it adds a retrospective capability that geophysical monitoring restricted to brief human timescales lacks. Although zircon age dispersion is seemingly a burden from the traditional perspective of an event-oriented geochronology, the increasing power to unravel the complexity of

accessory mineral crystallization in time and space also bears tremendous potential. In this review, we emphasized the need for improved statistical tools to adequately portray and interpret geochronological data and outlined potential strategies to advance conceptual models for dynamic magma systems. Progress in this regard requires the integration of empirical studies of volcanic and plutonic rocks that combine accessory mineral geochronology with other geological and petrological information such as (chrono-)stratigraphy, as well as correlative trace-element and isotope data, and lastly refinement of numerical simulations of the thermomechanical evolution of multiphase magmatic systems in dynamic settings. Further study of the thermal and compositional evolution of magmatic systems has direct implications for assessing volcanic hazards, constraining the heat sources of magmatic geothermal systems, and understanding the formation of ore deposits associated with magmatic intrusions.

APPENDIX. MagmaThermoKinematics.jl, AN OPEN-SOURCE SOFWARE PACKAGE TO SIMULATE THE THERMAL EVOLUTION OF MAGMATIC SYSTEMS

Modeling the thermal evolution of magmatic systems has a long tradition, and a range of commercial and non-commercial codes have been employed that intrude dikes and/or sills, and simulate the resulting thermal evolution of the intrusion and surrounding rocks. As the modeling assumptions, boundary conditions, and material parameters employed often differ between publications, it is not always straightforward to compare results from different studies. In addition, none of the software currently in use is available as an open source software, which makes it difficult to reproduce results or understand the finer implementation details.

To amend this situation, we have developed a new, open source, software package—MagmaThermoKinematics.jl (https://github.com/boriskaus/MagmaThermoKinematics.jl) (MTK)—using Julia (Bezanson et al., 2017; https://julialang.org), which can be employed to simulate the thermal evolution of magmatic systems. Julia is a high-level programming language that has some similarities to MATLAB or Python (and allows the creation of short, easy-to-understand code), but is compiled and therefore significantly faster than the above-mentioned interpreted languages. Moreover, it has outstanding support for multi-threaded parallel central processing units and GPUs, an excellent testing framework, and a fairly rich ecosystem of readily available packages that are written in a highly composable manner, which makes it easy to combine different packages.

The governing advection-diffusion equation relevant for the thermal evolution of magmatic systems with intruding magma is:

$$\rho c_p \left(\frac{\partial T}{\partial t} + v_j \frac{\partial T}{\partial x_j} \right) = \frac{\partial}{\partial x_i} \left(k \frac{\partial T}{\partial x_i} \right) + H_r + \rho Q_L \frac{\partial \phi_s}{\partial t}. \tag{A1}$$

Here, T denotes temperature [K], v host-rock velocity (induced by injecting a new sill), t time, $\phi_s = (1-\phi)$ the volume fraction of solid rock, ϕ the melt fraction (both dimensionless parameters between [0–1]), ρ density [kg m^{-3}], c_p heat capacity [J kg^{-1} K^{-1}], k conductivity [W m^{-1} K^{-1}], Q_L latent heat [J kg^{-1}], and H_r radioactive heat sources [W m^{-3}]. Many of the material properties can also be a function of temperature, which makes this a nonlinear equation.

In general, we solve Equation (A1) into two steps.

An *advection step* is applied only when a new sill is intruded, which happens every few 1000 years in most cases discussed here.

$$\frac{\partial T}{\partial t} + v_j \frac{\partial T}{\partial x_j} = 0. \tag{A2a}$$

We employ a Semi-Lagrangian advection scheme for this (e.g., Staniforth and Côté, 1991; Becker and Kaus, 2016), which takes into account that the host rock moves to create space for the intruding magma. The host-rock velocity is either set to be a constant below a horizontal sill (in the Geneva setup), can be elliptical in mass-conserving manner (in the UCLA-HD setup), or can be set from an elastic dike intrusion algorithm.

A *diffusion step* is applied more frequently:

$$\rho c_p \frac{\partial T}{\partial t} = \frac{\partial}{\partial x_i} \left(k \frac{\partial T}{\partial x_i} \right) + H_r + \rho Q_L \frac{\partial \phi_s}{\partial t}. \tag{A2b}$$

The last term in the equation involves the time derivative of the solid fraction. It turns out that this is numerically rather unstable and requires a very small time-step. Therefore, we apply the chain rule to this term and write this as:

$$\rho c_p \frac{\partial T}{\partial t} = \frac{\partial}{\partial x_i} \left(k \frac{\partial T}{\partial x_i} \right) + H_r + \rho Q_L \frac{\partial \phi_s}{\partial T} \frac{\partial T}{\partial t}$$

$$\rho c_p \frac{\partial T}{\partial t} + \rho Q_L \frac{\partial \phi}{\partial T} \frac{\partial T}{\partial t} = \frac{\partial}{\partial x_i} \left(k \frac{\partial T}{\partial x_i} \right) + H_r$$

$$\rho \left(c_p + Q_L \frac{\partial \phi}{\partial T} \right) \frac{\partial T}{\partial t} = \frac{\partial}{\partial x_i} \left(k \frac{\partial T}{\partial x_i} \right) + H_r. \tag{A3}$$

Here, we made use of the fact that $\partial \phi_s/\partial T = -\partial \phi/\partial T$. This formulation shows that the latent heat effect can be implemented by locally changing the heat capacity (e.g., Simpson, 2017; Gerya, 2019), which is numerically much more stable than

if using Equation (A2b) directly. It requires knowledge of the derivative of the melt fraction versus temperature, $\partial \phi/\partial T$, which can be computed analytically for most melt parameterizations and is obviously zero below the solidus and above the liquidus. Yet, an important aspect for stable numerical implementations is that this derivative must be continuous throughout the full temperature range. Some melting parameterizations result in a significant jump in $\partial \phi/\partial T$ around the solidus (or liquidus), which puts severe time-step restrictions on the numerical simulation. One solution is to apply a small amount of smoothening to existing parameterizations around the solidus and liquidus to enforce continuity. This is an option implemented in GeoParams.jl and allows larger time-steps to be taken while giving essentially the same results.

In MTK, the time-derivative in Equation (A3) is discretized in an *explicit* manner:

$$\rho \left(c_p + Q_L \frac{\partial \phi}{\partial T} \right) \frac{T^{n+1} - T^n}{\Delta t} = \frac{\partial}{\partial x_i} \left(k \frac{\partial T}{\partial x_i} \right) + H_r$$

$$T^{n+1} = T^n + \frac{\Delta t}{\rho \left(c_p + Q_L \frac{\partial \phi}{\partial T} \right)} \left(\frac{\partial}{\partial x_i} \left(k \frac{\partial T}{\partial x_i} \right) + H_r \right). \tag{A4}$$

The spatial derivative, $\frac{\partial}{\partial x_i} \left(k \frac{\partial T}{\partial x_i} \right)$, is implemented using a staggered grid finite difference scheme, which defines thermal conductivity in-between temperature grid points (e.g., Gerya, 2019). In 1-D, this would be:

$$\frac{\partial}{\partial x_i} \left(k \frac{\partial T}{\partial x_i} \right) \approx \frac{k^{i+\frac{1}{2}} \left(\frac{T^{i+1} - T^i}{\Delta x} \right) - k^{i-\frac{1}{2}} \left(\frac{T^i - T^{i-1}}{\Delta x} \right)}{\Delta x}, \tag{A5}$$

where Δx is the (constant) spacing between temperature grid-nodes that are defined at points indicated with a superscript i. The thermal conductivity is physically located at a point that is exactly in between two temperature grid points. In case of temperature-dependent conductivity, we first interpolate temperature to that same grid point, i.e., $T^{i+\frac{1}{2}} = \frac{T^{i+1} + T^i}{2}$.

The advantage of employing the explicit approach is that it results in an algorithm that can be quite efficiently implemented on the GPU, for example by using the ParallelStencil.jl Julia package (e.g., Räss et al., 2022). A disadvantage is that there are time-step restrictions due to the Courant-Friedrichs-Lewy criteria, which state that:

$$\frac{\max(\kappa) \Delta t}{\min\left(\Delta x^2, \Delta y^2, \Delta z^2 \right)} < 0.5, \tag{A6}$$

where $\kappa = \frac{k}{\rho \left(c_p + Q_L \frac{\partial \phi}{\partial T} \right)}$ is the thermal diffusivity and Δx, Δy, Δz the grid spacing in three directions (for 3-D). In case material parameters are spatially variable or depend on temperature, one can use an upper bound to estimate κ.

Equation A4 works for the case that parameters are independent of temperature, which is generally not the case (ϕ and $\partial \phi/\partial T$ obviously depends on T). Therefore, one typically has to employ *nonlinear* iterations. In the general case that ρ, c_p, k, and $\partial \phi/\partial T$ depend on T, this gives:

$$T^{n+1,it+1} = T^n + \frac{\Delta t}{\rho(\tilde{T}) \left(c_p(\tilde{T}) + Q_L \frac{\partial \phi}{\partial T}(\tilde{T}) \right)} \left(\frac{\partial}{\partial x_i} \left(k(\tilde{T}) \frac{\partial T^n}{\partial x_i} \right) \nabla (\nabla T^n) + H_r \right). \tag{A7}$$

We employ dampened Picard iterations, which are computed as:

$$\tilde{T} = \omega T^{n+1,it+1} + (1-\omega)T^{n+1,it}, \tag{A8}$$

where $\omega = [0 - 1]$ is a dampening parameter and the superscript ^{it} denotes the iteration step. Equations (A7) and (A8) are solved until the relative difference between subsequent iteration steps,

$$err = \frac{\max(abs(T^{n+1,it+1} - T^{n+1,it}))}{\max\left(abs\left(T^{n+1,it+1}\right)\right)}, \tag{A9}$$

becomes smaller than a predefined tolerance (e.g., 10^{-5}).

In MTK, the governing Equations (A7) and (A8) are implemented in 2-D, 2-D axisymmetric, and 3-D geometries. Finite difference stencils are implemented using ParallelStencil. jl (https://github.com/omlins/ParallelStencil.jl), which is a Julia package for efficient stencil computations that allows the simulations to be run on either parallel multicore processors or on GPU cards.

Parameterizations for material properties (such as thermal conductivity, melt fraction, or heat capacity) are implemented in a separate package (GeoParams.jl[1], https://github.com /JuliaGeodynamics/GeoParams.jl), which allows reuse of those in independent software packages (while having to implement and test them only once). We provide a range of melt-intrusion algorithms, which include elliptical or cylindrical geometries, or follow the analytical solution for intrusion of a dill/dike in an elastic half-space. Tracers can be injected to track the thermal evolution of the intruded magma and host rock, and there is a simple mechanism to change the type of material properties employed (e.g., using a temperature-dependent conductivity instead of a constant value). Both flux and isothermal bottom boundary conductions can be implemented.

The results of each calculation comprise, besides the thermal field, time-temperature paths on every tracer, which can be used in a postprocessing step to compute zircon age data (using a Julia implementation of R-scripts provided by Weber et al., 2020, which is provided in GeoParams.jl). The file example 2D_ZASSy.jl reproduces the results shown in Figures 11 and 12, which include both end-member models.

Petrological-thermal modeling studies of magmatic systems often use slightly different assumptions, such as constant versus temperature-dependent conductivity, 2-D versus axisymmetric geometries, or employ different melt-curve parameterizations. It is often unclear what the impact of those assumptions will be on the final temperature distributions of the magmatic system. For that reason, we performed a sensitivity analysis using the two end-member scenarios described in the manuscript (Figs. 11 and 12). In each case, we kept all parameters the same as in the reference simulation but changed one parameter. We report the final temperature profiles in the center and at the side of the domain. Results are shown in Fig. S1 (see text footnote 1) and demonstrate that the numerical parameters (such as resolution or time-step) only have a minor effect, but that latent heating and temperature-dependent conductivity can have an impact that is equal to or greater than reducing the magma flux for the sill under-accretion setup, whereas they have little impact on the central intrusion setup. This is likely because the central intrusion setup has nearly reached a steady state, where magma intrusion balances thermal diffusion and the partially molten zone remains more or less constant in size. The sill under-accretion case, on the other hand, has a partially molten zone that still grows in space after 1.5 m.y. (Fig. S1).

REFERENCES CITED

Angeles-De La Torre, C.A., Schmitt, A.K., Lovera, O.M., Gassert, H., Gerdes, A., and Harvey, J.C., 2023, A common magma source for plutonic and volcanic rocks of the Geysers geothermal field, California: Volume and intrusive history derived from zircon: Chemical Geology, v. 624, https://doi .org/10.1016/j.chemgeo.2023.121414.

Annen, C., 2009, From plutons to magma chambers: Thermal constraints on the accumulation of eruptible silicic magma in the upper crust: Earth and Planetary Science Letters, v. 284, no. 3–4, p. 409–416, https://doi.org/10.1016/j.epsl.2009.05.006.

Annen, C., Blundy, J., and Sparks, R., 2006, The genesis of intermediate and silicic magmas in deep crustal hot zones: Journal of Petrology, v. 47, no. 3, p. 505–539, https://doi.org /10.1093/petrology/egi084.

Annen, C., Blundy, J.D., Leuthold, J., and Sparks, R.S.J., 2015, Construction and evolution of igneous bodies: Towards an integrated perspective of crustal magmatism: Lithos, v. 230, p. 206–221, https://doi.org/10.1016/j.lithos.2015.05.008.

Bachmann, O., and Bergantz, G.W., 2006, Gas percolation in upper-crustal silicic crystal mushes as a mechanism for upward heat advection and rejuvenation of near-solidus magma bodies: Journal of Volcanology and Geothermal Research, v. 149, no. 1–2, p. 85–102, https://doi.org/10.1016 /j.jvolgeores.2005.06.002.

Bachmann, O., Oberli, F., Dungan, M., Meier, M., Mundil, R., and Fischer, H., 2007, $^{40}Ar/^{39}Ar$ and U–Pb dating of the Fish Canyon magmatic system, San Juan Volcanic field, Colorado: Evidence for an extended crystallization history: Chemical Geology, v. 236, no. 1–2, p. 134–166, https://doi.org/10.1016 /j.chemgeo.2006.09.005.

Bacon, C.R., 1989, Crystallization of accessory phases in magmas by local saturation adjacent to phenocrysts: Geochimica et Cosmochimica Acta, v. 53, no. 5, p. 1055–1066, https://doi .org/10.1016/0016-7037(89)90210-X.

Baker, D.R., Conte, A., Freda, C., and Ottolini, L., 2002, The effect of halogens on Zr diffusion and zircon dissolution in hydrous metaluminous granitic melts: Contributions to Mineralogy and Petrology, v. 142, no. 6, p. 666–678, https:// doi.org/10.1007/s00410-001-0328-3.

Barboni, M., Boehnke, P., Schmitt, A.K., Harrison, T.M., Shane, P., Bouvier, A.-S., and Baumgartner, L., 2016, Warm storage for arc magmas: Proceedings of the National Academy of Sciences of the United States of America, v. 113, no. 49, p. 13,959–13,964, https://doi.org/10.1073/pnas.1616129113.

Becker, T.W., and Kaus, B.J.P., 2016, Numerical modeling of Earth systems, an introduction to computational methods with focus on solid Earth applications of continuum mechanics: University of Southern California Lecture Notes, http://www-udc.ig.utexas.edu/external/becker/preprints /Geodynamics557.pdf (last accessed April 2023).

Bezanson, J., Edelman, A., Karpinski, S., and Shah, V.B., 2017, Julia: A fresh approach to numerical computing: SIAM Review, v. 59, p. 65–98, https://doi.org/10.1137/141000671.

Bindeman, I.N., and Melnik, O.E., 2016, Zircon survival, rebirth and recycling during crustal melting, magma crystallization, and mixing based on numerical modelling: Journal of Petrology, v. 57, no. 3, p. 437–460, https://doi.org/10.1093 /petrology/egw013.

Blatter, D.L., and Carmichael, I.S., 2001, Hydrous phase equilibria of a Mexican high-silica andesite: A candidate for a mantle origin?: Geochimica et Cosmochimica Acta, v. 65, no. 21, p. 4043–4065, https://doi.org/10.1016/S0016-7037(01)00708-6.

Boehnke, P, Watson, E.B., Trail, D., Harrison, T.M., and Schmitt, A.K., 2013, Zircon saturation re-revisited: Chemical Geology, v. 351, p. 324–334, https://doi.org/10.1016/j.chemgeo .2013.05.028.

Borisov, A., and Aranovich, L., 2019, Zircon solubility in silicate melts: New experiments and probability of zircon crystallization in deeply evolved basic melts: Chemical Geology, v. 510, p. 103–112, https://doi.org/10.1016/j.chemgeo.2019.02.019.

Botev, Z.I., Grotowski, J.F., and Kroese, D.P., 2010, Kernel density estimation via diffusion: Annals of Statistics, v. 38, no. 5, p. 2916–2957, https://doi.org/10.1214/10-AOS799.

Bouilhol, P., Connolly, J.A., and Burg, J.-P., 2011, Geological evidence and modeling of melt migration by porosity waves in the sub-arc mantle of Kohistan (Pakistan): Geology, v. 39, no. 12, p. 1091–1094, https://doi.org/10.1130/G32219.1.

Caricchi, L., Simpson, G., and Schaltegger, U., 2014, Zircons reveal magma fluxes in the Earth's crust: Nature, v. 511, no. 7510, p. 457–461, https://doi.org/10.1038/nature13532.

Caricchi, L., Simpson, G., and Schaltegger, U., 2016, Estimates of volume and magma input in crustal magmatic systems from zircon geochronology: The effect of modeling assumptions and system variables: Frontiers of Earth Science, v. 4, p. 48, https://doi.org/10.3389/feart.2016.00048.

Carrigan, C.R., 1988, Biot number and thermos bottle effect: Implications for magma-chamber convection: Geology, v. 16, no. 9, p. 771–774, https://doi.org/10.1130/0091-7613(1988)016 <0771:BNATBE>2.3.CO;2.

Cherniak, D., and Watson, E., 2001, Pb diffusion in zircon: Chemical Geology, v. 172, no. 1–2, p. 5–24, https://doi.org/10.1016 /S0009-2541(00)00233-3.

Cherniak, D.J., Hanchar, J.M., and Watson, E.B., 1997, Diffusion of tetravalent cations in zircon: Contributions to Mineralogy and Petrology, v. 127, no. 4, p. 383–390, https://doi.org /10.1007/s004100050287.

Claiborne, L.L., Miller, C., Walker, B., Wooden, J., Mazdab, F., and Bea, F., 2006, Tracking magmatic processes through Zr/Hf ratios in rocks and Hf and Ti zoning in zircons: An example from the Spirit Mountain batholith, Nevada: Mineralogical Magazine, v. 70, no. 5, p. 517–543, https://doi.org/10.1180 /0026461067050348.

Claiborne, L.L., Miller, C.F., and Wooden, J.L., 2010, Trace element composition of igneous zircon: A thermal and compositional record of the accumulation and evolution of a large silicic batholith, Spirit Mountain, Nevada: Contributions to Mineralogy and Petrology, v. 160, no. 4, p. 511–531, https://doi .org/10.1007/s00410-010-0491-5.

Coleman, D.S., Gray, W., and Glazner, A.F., 2004, Rethinking the emplacement and evolution of zoned plutons: Geochronologic evidence for incremental assembly of the Tuolumne Intrusive Suite, California: Geology, v. 32, no. 5, p. 433–436, https://doi.org/10.1130/G20220.1.

Costa, F., Shea, T., and Ubide, T., 2020, Diffusion chronometry and the timescales of magmatic processes: Nature Reviews: Earth & Environment, v. 1, no. 4, p. 201–214, https://doi.org /10.1038/s43017-020-0038-x.

Coutts, D.S., Matthews, W.A., and Hubbard, S.M., 2019, Assessment of widely used methods to derive depositional ages from detrital zircon populations: Geoscience Frontiers, v. 10, no. 4, p. 1421–1435, https://doi.org/10.1016/j.gsf.2018.11.002.

Crisp, J.A., 1984, Rates of magma emplacement and volcanic output: Journal of Volcanology and Geothermal Research, v. 20, no. 3–4, p. 177–211, https://doi.org/10.1016/0377-0273(84)90039-8.

Crowley, J.L., Schoene, B., and Bowring, S., 2007, U-Pb dating of zircon in the Bishop Tuff at the millennial scale: Geology, v. 35, no. 12, p. 1123–1126, https://doi.org/10.1130/G24017A.1.

Curry, A., Caricchi, L., and Lipman, P.W., 2021, Magmatic evolution of zoned and unzoned ignimbrites: Evidence for a complex crustal architecture feeding four rapid-sequence, caldera-forming eruptions in the San Juan Mountains, Colorado: Journal of Petrology, v. 62, no. 5, https://doi.org/10.1093/petrology/egab006.

Deckart, K., Godoy, E., Bertens, A., Jerez, D., and Saeed, A., 2010, Barren Miocene granitoids in the Central Andean metallogenic belt, Chile: Geochemistry and Nd-Hf and U-Pb isotope systematics: Andean Geology, v. 37, no. 1, p. 1–31, https://doi.org/10.4067/S0718-71062010000100001.

Degruyter, W., and Huber, C., 2014, A model for eruption frequency of upper crustal silicic magma chambers: Earth and Planetary Science Letters, v. 403, p. 117–130, https://doi.org/10.1016/j.epsl.2014.06.047.

Dodson, M., Compston, W., Williams, I., and Wilson, J., 1988, A search for ancient detrital zircons in Zimbabwean sediments: Journal of the Geological Society, v. 145, no. 6, p. 977–983, https://doi.org/10.1144/gsjgs.145.6.0977.

Dufek, J., and Bergantz, G.W., 2005, Lower crustal magma genesis and preservation: A stochastic framework for the evaluation of basalt–crust interaction: Journal of Petrology, v. 46, no. 11, p. 2167–2195, https://doi.org/10.1093/petrology/egi049.

Fedele, L., Tarzia, M., Belkin, H.E., DeVivo, B., Lima, A., and Lowenstern, J.B., 2006, Magmatic-hydrothermal fluid interaction and mineralization in alkali-syenite nodules from the Breccia Museo pyroclastic deposit, Naples, Italy, in De Vivo, B., ed., Volcanism in the Campania Plain-Vesuvius Campi Flegrei and Ignimbrites: Elsevier, Developments in Volcanology, v. 9, p. 125–161.

Flaherty, T., Druitt, T.H., Tuffen, H., Higgins, M.D., Costa, F., and Cadoux, A., 2018, Multiple timescale constraints for high-flux magma chamber assembly prior to the late Bronze Age eruption of Santorini (Greece): Contributions to Mineralogy and Petrology, v. 173, no. 9, https://doi.org/10.1007/s00410-018-1490-1.

Friedrichs, B., Schmitt, A.K., Lovera, O.M., and Atıcı, G., 2021, Zircon as a recorder of contrasting magma recharge and eruptive recurrence patterns: Earth and Planetary Science Letters, v. 571, https://doi.org/10.1016/j.epsl.2021.117104.

Galbraith, R.F., 1990, The radial plot: Graphical assessment of spread in ages: International Journal of Radiation Applications and Instrumentation. Part D: Nuclear Tracks and Radiation Measurements, v. 17, no. 3, p. 207–214, https://doi.org/10.1016/1359-0189(90)90036-W.

Gebauer, S.K., Schmitt, A.K., Pappalardo, L., Stockli, D.F., and Lovera, O.M., 2014, Crystallization and eruption ages of Breccia Museo (Campi Flegrei caldera, Italy) plutonic clasts and their relation to the Campanian ignimbrite: Contributions to Mineralogy and Petrology, v. 167, no. 1, https://doi.org/10.1007/s00410-013-0953-7.

Gervasoni, F., Klemme, S., Rocha-Júnior, E.R., and Berndt, J., 2016, Zircon saturation in silicate melts: A new and improved model for aluminous and alkaline melts: Contributions to Mineralogy and Petrology, v. 171, no. 3, https://doi.org/10.1007/s00410-016-1227-y.

Gerya, T., 2019, Introduction to Numerical Geodynamic Modelling: Cambridge, UK, Cambridge University Press, 484 p., https://doi.org/10.1017/9781316534243.

Giordano, G., and Caricchi, L., 2022, Determining the state of activity of transcrustal magmatic systems and their volcanoes: Annual Review of Earth and Planetary Sciences, v. 50, p. 231–259, https://doi.org/10.1146/annurev-earth-032320-084733.

Glazner, A.F., and Sadler, P.M., 2016, Estimating the duration of geologic intervals from a small number of age determinations: A challenge common to petrology and paleobiology: Geochemistry, Geophysics, Geosystems, v. 17, no. 12, p. 4892–4898, https://doi.org/10.1002/2016GC006542.

Gutiérrez, F., Payacán, I., Szymanowski, D., Guillong, M., Bachmann, O., and Parada, M., 2018, Lateral magma propagation during the emplacement of La Gloria Pluton, central Chile: Geology, v. 46, no. 12, p. 1051–1054, https://doi.org/10.1130/G45361.1.

Harrison, T.M., Watson, E.B., and Aikman, A.B., 2007, Temperature spectra of zircon crystallization in plutonic rocks: Geology, v. 35, no. 7, p. 635–638, https://doi.org/10.1130/G23505A.1.

Hayman, N.W., Rioux, M., Anma, R., Tani, K., Dunkley, D.J., Crowley, J., and Schmitz, M., 2019, Accretion and oxidation of a superfast-spread axial melt lens: TIMS and SIMS zircon analyses of the IODP Hole 1256D gabbros: Lithos, v. 348, https://doi.org/10.1016/j.lithos.2019.105184.

Hou, T., Botcharnikov, R., Moulas, E., Just, T., Berndt, J., Koepke, J., Zhang, Z., Wang, M., Yang, Z., and Holtz, F., 2020, Kinetics of Fe–Ti oxide re-equilibration in magmatic systems: Implications for thermo-oxybarometry: Journal of Petrology, v. 61, no. 11–12, https://doi.org/10.1093/petrology/egaa116.

Huber, C., Bachmann, O., and Manga, M., 2009, Homogenization processes in silicic magma chambers by stirring and mushification (latent heat buffering): Earth and Planetary Science Letters, v. 283, no. 1–4, p. 38–47, https://doi.org/10.1016/j.epsl.2009.03.029.

Jackson, M., Gallagher, K., Petford, N., and Cheadle, M., 2005, Towards a coupled physical and chemical model for tonalite–trondhjemite–granodiorite magma formation: Lithos, v. 79, no. 1–2, p. 43–60, https://doi.org/10.1016/j.lithos.2004.05.004.

Jackson, M., Blundy, J., and Sparks, R., 2018, Chemical differentiation, cold storage and remobilization of magma in the Earth's crust: Nature, v. 564, no. 7736, p. 405–409, https://doi.org/10.1038/s41586-018-0746-2.

Jackson, M.D., Cheadle, M.J., and Atherton, M.P., 2003, Quantitative modeling of granitic melt generation and segregation in the continental crust: Journal of Geophysical Research: Solid Earth, v. 108, no. B7, https://doi.org/10.1029/2001JB001050.

Karakas, O., Degruyter, W., Bachmann, O., and Dufek, J., 2017, Lifetime and size of shallow magma bodies controlled by crustal-scale magmatism: Nature Geoscience, v. 10, no. 6, p. 446–450, https://doi.org/10.1038/ngeo2959.

Katz, R.F., Jones, D.W.R., Rudge, J.F., and Keller, T., 2022, Physics of melt extraction from the mantle: Speed and style: Annual Review of Earth and Planetary Sciences, v. 50, p. 507–540, https://doi.org/10.1146/annurev-earth-032320-083704.

Keller, C.B., Schoene, B., and Samperton, K.M., 2018, A stochastic sampling approach to zircon eruption age interpretation: Geochemical Perspectives Letters, v. 8, https://doi.org/10.7185/geochemlet.1826.

Keller, T., and Katz, R.F., 2016, The role of volatiles in reactive melt transport in the asthenosphere: Journal of Petrology, v. 57, no. 6, p. 1073–1108, https://doi.org/10.1093/petrology/egw030.

Keller, T., and Suckale, J., 2019, A continuum model of multiphase reactive transport in igneous systems: Geophysical Journal International, v. 219, no. 1, p. 185–222, https://doi.org/10.1093/gji/ggz287.

Keller, T., May, D.A., and Kaus, B.J., 2013, Numerical modelling of magma dynamics coupled to tectonic deformation of lithosphere and crust: Geophysical Journal International, v. 195, no. 3, p. 1406–1442, https://doi.org/10.1093/gji/ggt306.

Keller, T., Katz, R.F., and Hirschmann, M.M., 2017, Volatiles beneath mid-ocean ridges: Deep melting, channelised transport, focusing, and metasomatism: Earth and Planetary Science Letters, v. 464, p. 55–68, https://doi.org/10.1016/j.epsl.2017.02.006.

Kelsey, D., and Powell, R., 2011, Progress in linking accessory mineral growth and breakdown to major mineral evolution in metamorphic rocks: A thermodynamic approach in the Na_2O-CaO-K_2O-FeO-MgO-Al_2O_3-SiO_2-H_2O-TiO_2-ZrO_2 system: Journal of Metamorphic Geology, v. 29, no. 1, p. 151–166, https://doi.org/10.1111/j.1525-1314.2010.00910.x.

Kent, A.J., and Cooper, K.M., 2018, How well do zircons record the thermal evolution of magmatic systems?: Geology, v. 46, no. 2, p. 111–114, https://doi.org/10.1130/G39690.1.

Kohn, M.J., 2016, Metamorphic chronology — a tool for all ages: Past achievements and future prospects: The American Mineralogist, v. 101, no. 1, p. 25–42, https://doi.org/10.2138/am-2016-5146.

Kohn, M.J., Corrie, S.L., and Markley, C., 2015, The fall and rise of metamorphic zircon: The American Mineralogist, v. 100, no. 4, p. 897–908, https://doi.org/10.2138/am-2015-5064.

Kryza, R., Crowley, Q.G., Larionov, A., Pin, C., Oberc-Dziedzic, T., and Mochnacka, K., 2012, Chemical abrasion applied to SHRIMP zircon geochronology: An example from the Variscan Karkonosze Granite (Sudetes, SW Poland): Gondwana Research, v. 21, no. 4, p. 757–767, https://doi.org/10.1016/j.gr.2011.07.007.

Lasaga, A.C., 1986, Metamorphic reaction rate laws and development of isograds: Mineralogical Magazine, v. 50, no. 357, p. 359–373, https://doi.org/10.1180/minmag.1986.050.357.02.

Liao, Y., Soule, S.A., Jones, M., and Le Mével, H., 2021, The mechanical response of a magma chamber with porovisco-elastic crystal mush: Journal of Geophysical Research: Solid Earth, v. 126, no. 4, https://doi.org/10.1029/2020JB019395.

Linnen, R.L., and Keppler, H., 2002, Melt composition control of Zr/Hf fractionation in magmatic processes: Geochimica et Cosmochimica Acta, v. 66, no. 18, p. 3293–3301, https://doi.org/10.1016/S0016-7037(02)00924-9.

Liu, P-P., Caricchi, L., Chung, S.-L., Li, X.-H., Li, Q.-L., Zhou, M.-F., Lai, Y.-M., Ghani, A.A., Sihotang, T., and Sheldrake, T.E., 2021, Growth and thermal maturation of the Toba magma reservoir: Proceedings of the National Academy of Sciences of the United States of America, v. 118, no. 45, https://doi.org/10.1073/pnas.2101695118.

Lubbers, J., Deering, C., and Bachmann, O., 2020, Genesis of rhyolitic melts in the upper crust: Fractionation and

remobilization of an intermediate cumulate at Lake City caldera, Colorado, USA: Journal of Volcanology and Geothermal Research, v. 392, https://doi.org/10.1016/j.jvolgeores.2019.106750.

Lukács, R., Harangi, S., Guillong, M., Bachmann, O., Fodor, L., Buret, Y., Dunkl, I., Sliwinski, J., von Quadt, A., and Peytcheva, I., 2018, Early to mid-Miocene syn-extensional massive silicic volcanism in the Pannonian Basin (East-Central Europe): Eruption chronology, correlation potential and geodynamic implications: Earth-Science Reviews, v. 179, p. 1–19, https://doi.org/10.1016/j.earscirev.2018.02.005.

Lukács, R., Caricchi, L., Schmitt, A.K., Bachmann, O., Karakas, O., Guillong, M., Molnár, K., Seghedi, I., and Harangi, S., 2021, Zircon geochronology suggests a long-living and active magmatic system beneath the Ciomadul volcanic dome field (eastern-central Europe): Earth and Planetary Science Letters, v. 565, https://doi.org/10.1016/j.epsl.2021.116965.

Marillo-Sialer, E., Woodhead, J., Hanchar, J., Reddy, S., Greig, A., Hergt, J., and Kohn, B., 2016, An investigation of the laser-induced zircon 'matrix effect': Chemical Geology, v. 438, p. 11–24, https://doi.org/10.1016/j.chemgeo.2016.05.014.

Marxer, F., and Ulmer, P., 2019, Crystallisation and zircon saturation of calc-alkaline tonalite from the Adamello Batholith at upper crustal conditions: An experimental study: Contributions to Mineralogy and Petrology, v. 174, no. 10, https://doi.org/10.1007/s00410-019-1619-x.

Mattinson, J.M., 2005, Zircon U–Pb chemical abrasion ("CA-TIMS") method: Combined annealing and multi-step partial dissolution analysis for improved precision and accuracy of zircon ages: Chemical Geology, v. 220, no. 1–2, p. 47–66, https://doi.org/10.1016/j.chemgeo.2005.03.011.

Mehnert, H., Lipman, P., and Steven, T., 1973, Age of the Lake City caldera and related Sunshine Peak Tuff, western San Juan Mountains: Colorado: Isochron-West, v. 6, p. 31–33.

Melnik, O.E., Utkin, I.S., and Bindeman, I.N., 2021, Magma chamber formation by dike accretion and crustal melting: 2-D thermo-compositional model with emphasis on eruptions and implication for zircon records: Journal of Geophysical Research: Solid Earth, v. 126, https://doi.org/10.1029/2021JB023008.

Miller, J.S., Matzel, J.E., Miller, C.F., Burgess, S.D., and Miller, R.B., 2007, Zircon growth and recycling during the assembly of large, composite arc plutons: Journal of Volcanology and Geothermal Research, v. 167, no. 1–4, p. 282–299, https://doi.org/10.1016/j.jvolgeores.2007.04.019.

Oberli, F., Fischer, H., and Meier, M., 1990, High-resolution ^{238}U–^{206}Pb zircon dating of Tertiary bentonites and Fish Canyon Tuff; a test for age "concordance" by single-crystal analysis, in Proceedings, Seventh International Conference on Geochronology, Cosmochronology and Isotope Geology: Geological Society of Australia Special Publication 27, p. 74.

Pamukçu, A.S., Schoene, B., Deering, C.D., Keller, C.B., and Eddy, M.P., 2022, Volcano-pluton connections at the Lake City magmatic center (Colorado, USA): Geosphere, v. 18, no. 5, p. 1435–1452, https://doi.org/10.1130/GES02467.1.

Pullen, A., Ibáñez-Mejía, M., Gehrels, G.E., Ibáñez-Mejía, J.C., and Pecha, M., 2014, What happens when n= 1000? Creating large-n geochronological datasets with LA-ICP-MS for geologic investigations: Journal of Analytical Atomic Spectrometry, v. 29, no. 6, p. 971–980, https://doi.org/10.1039/C4JA00024B.

Räss, L., Utkin, I., Duretz, T., Omlin, S., and Podladchikov, Y.Y., 2022, Assessing the robustness and scalability of the accelerated pseudo-transient method: Geoscientific Model Development, v. 15, p. 5757–5786, https://doi.org/10.5194/gmd-15-5757-2022.

Ratschbacher, B.C., Keller, C.B., Schoene, B., Paterson, S.R., Anderson, J.L., Okaya, D., Putirka, K., and Lippoldt, R., 2018, A new workflow to assess emplacement duration and melt residence time of compositionally diverse magmas emplaced in a sub-volcanic reservoir: Journal of Petrology, v. 59, no. 9, p. 1787–1809, https://doi.org/10.1093/petrology/egy079.

Reid, M.R., Coath, C.D., Harrison, T.M., and McKeegan, K.D., 1997, Prolonged residence times for the youngest rhyolites associated with Long Valley Caldera: ^{230}Th–^{238}U ion microprobe dating of young zircons: Earth and Planetary Science Letters, v. 150, no. 1–2, p. 27–39, https://doi.org/10.1016/S0012-821X(97)00077-0.

Riel, N., Bouilhol, P., van Hunen, J., Cornet, J., Magni, V., Grigorova, V., and Velic, M., 2019, Interaction between mantle-derived magma and lower arc crust: Quantitative reactive melt flow modelling using Styx, in Ferraro, S. Lanari, P., Goncalves, P., and Grosch, E.P., eds., Metamorphic Geology: Microscale to Mountain Belts: Geological Society, London, Special Publication 478, no. 1, p. 65–87, https://doi.org/10.1144/SP478.6.

Riel, N., Kaus, B.J.P., Green, E.C.R, and Berlie, N., 2022, MAGEMin, an efficient Gibbs energy minimizer: Application to igneous systems: Geochemistry, Geophysics, Geosystems, v. 23, no. 7, https://doi.org/10.1029/2022GC010427.

Rubatto, D., 2017, Zircon: The metamorphic mineral: Reviews in Mineralogy and Geochemistry, v. 83, no. 1, p. 261–295, https://doi.org/10.2138/rmg.2017.83.9.

Rummel, L., Kaus, B.J., Baumann, T.S., White, R.W., and Riel, N., 2020, Insights into the compositional evolution of crustal magmatic systems from coupled petrological-geodynamical models: Journal of Petrology, v. 61, no. 2, https://doi.org/10.1093/petrology/egaa029.

Sambridge, M., and Compston, W., 1994, Mixture modeling of multi-component data sets with application to ion-probe zircon ages: Earth and Planetary Science Letters, v. 128, no. 3–4, p. 373–390, https://doi.org/10.1016/0012-821X(94)90157-0.

Samperton, K.M., Bell, E.A., Barboni, M., Keller, C.B., and Schoene, B., 2017, Zircon age-temperature-compositional spectra in plutonic rocks: Geology, v. 45, no. 11, p. 983–986, https://doi.org/10.1130/G38645.1.

Satow, C., Gudmundsson, A., Gertisser, R., Ramsey, C.B., Bazargan, M., Pyle, D.M., Wulf, S., Miles, A.J., and Hardiman, M., 2021, Eruptive activity of the Santorini Volcano controlled by sea-level rise and fall: Nature Geoscience, v. 14, no. 8, p. 586–592, https://doi.org/10.1038/s41561-021-00783-4.

Schaltegger, U., 2007, Hydrothermal zircon: Elements, v. 3, no. 1, p. 51–79, https://doi.org/10.2113/gselements.3.1.51.

Schaltegger, U., Schmitt, A., and Horstwood, M., 2015, U–Th–Pb zircon geochronology by ID-TIMS, SIMS, and laser ablation ICP-MS: Recipes, interpretations, and opportunities: Chemical Geology, v. 402, p. 89–110, https://doi.org/10.1016/j.chemgeo.2015.02.028.

Schmitt, A.K., 2011, Uranium series accessory crystal dating of magmatic processes: Annual Review of Earth and Planetary Sciences, v. 39, p. 321–349, https://doi.org/10.1146/annurev-earth-040610-133330.

Schmitt, A.K., and Vazquez, J.A., 2017, Secondary ionization mass spectrometry analysis in petrochronology: Reviews in Mineralogy and Geochemistry, v. 83, no. 1, p. 199–230, https://doi.org/10.2138/rmg.2017.83.7.

Schmitt, A.K., Stockli, D.F., Lindsay, J.M., Robertson, R., Lovera, O.M., and Kislitsyn, R., 2010, Episodic growth and homogenization of plutonic roots in arc volcanoes from combined U–Th and (U–Th)/He zircon dating: Earth and Planetary Science Letters, v. 295, no. 1–2, p. 91–103, https://doi.org/10.1016/j.epsl.2010.03.028.

Schmitt, A.K., Perfit, M.R., Rubin, K.H., Stockli, D.F., Smith, M.C., Cotsonika, L.A., Zellmer, G.F., Ridley, W.I., and Lovera, O.M., 2011, Rapid cooling rates at an active mid-ocean ridge from zircon thermochronology: Earth and Planetary Science Letters, v. 302, no. 3–4, p. 349–358, https://doi.org/10.1016/j.epsl.2010.12.022.

Schmitt, A.K., Klitzke, M., Gerdes, A., and Schäfer, C., 2017, Zircon hafnium–oxygen isotope and trace element petrochronology of intraplate volcanic rocks from the Eifel (Germany) and implications for mantle versus crustal origins of zircon megacrysts: Journal of Petrology, v. 58, no. 9, p. 1841–1870, https://doi.org/10.1093/petrology/egx075.

Schoene, B., 2014, 4.10-U–Th–Pb geochronology, in Holland, H.D., and Turekian, K.K., eds., Treatise on Geochemistry: Elsevier, v. 4, p. 341–378, https://doi.org/10.1016/B978-0-08-095975-7.00310-7.

Shane, P., Storm, S., Schmitt, A.K., and Lindsay, J.M., 2012, Timing and conditions of formation of granitoid clasts erupted in recent pyroclastic deposits from Tarawera Volcano (New Zealand): Lithos, v. 140, p. 1–10, https://doi.org/10.1016/j.lithos.2012.01.012.

Shao, T., Xia, Y., Ding, X., Cai, Y., and Song, M., 2020, Zircon saturation model in silicate melts: A review and update: Acta Geochimica, v. 39, no. 3, p. 387–403, https://doi.org/10.1007/s11631-019-00384-4.

Simpson, G., 2017, Practical Finite Element Modeling in Earth Science Using Matlab: Chichester, UK, John Wiley & Sons, Ltd., https://doi.org/10.1002/9781119248644.

Sliwinski, J.T., Guillong, M., Liebske, C., Dunkl, I., Von Quadt, A., and Bachmann, O., 2017, Improved accuracy of LA-ICP-MS U-Pb ages of Cenozoic zircons by alpha dose correction: Chemical Geology, v. 472, p. 8–21, https://doi.org/10.1016/j.chemgeo.2017.09.014.

Sliwinski, J.T., Guillong, M., Lipman, P.W., Zimmerer, M.J., Deering, C., and Bachmann, O., 2022, Zircon U-Pb geochronology and trace element dataset from the Southern Rocky Mountain Volcanic Field, Colorado, USA: Data in Brief, v. 43, https://doi.org/10.1016/j.dib.2022.108362.

Solano, J., Jackson, M., Sparks, R., Blundy, J.D., and Annen, C., 2012, Melt segregation in deep crustal hot zones: A mechanism for chemical differentiation, crustal assimilation and the formation of evolved magmas: Journal of Petrology, v. 53, no. 10, p. 1999–2026, https://doi.org/10.1093/petrology/egs041.

Spera, F.J., and Bohrson, W.A., 2001, Energy-constrained open-system magmatic processes I: General model and energy-constrained assimilation and fractional crystallization (EC-AFC) formulation: Journal of Petrology, v. 42, no. 5, p. 999–1018, https://doi.org/10.1093/petrology/42.5.999.

Staniforth, A., and Côté, J., 1991, Semi-Lagrangian integration schemes for atmospheric models—A review: Monthly

Weather Review, v. 119, no. 9, p. 2206–2223, https://doi.org/10.1175/1520-0493(1991)119<2206:SLISFA>2.0.CO;2.

Storm, S., Shane, P., Schmitt, A.K., and Lindsay, J.M., 2012, Decoupled crystallization and eruption histories of the rhyolite magmatic system at Tarawera volcano revealed by zircon ages and growth rates: Contributions to Mineralogy and Petrology, v. 163, no. 3, p. 505–519, https://doi.org/10.1007/s00410-011-0682-8.

Szymanowski, D., Forni, F., Wolff, J.A., and Ellis, B.S., 2020, Modulation of zircon solubility by crystal–melt dynamics: Geology, v. 48, no. 8, p. 798–802, https://doi.org/10.1130/G47405.1.

Tierney, C.R., Schmitt, A.K., Lovera, O.M., and de Silva, S.L., 2016, Voluminous plutonism during volcanic quiescence revealed by thermochemical modeling of zircon: Geology, v. 44, no. 8, p. 683–686, https://doi.org/10.1130/G37968.1.

Townsend, M., 2022, Linking surface deformation to thermal and mechanical magma chamber processes: Earth and Planetary Science Letters, v. 577, https://doi.org/10.1016/j.epsl.2021.117272.

Townsend, M., and Huber, C., 2020, A critical magma chamber size for volcanic eruptions: Geology, v. 48, no. 5, p. 431–435, https://doi.org/10.1130/G47045.1.

Townsend, M., Huber, C., Degruyter, W., and Bachmann, O., 2019, Magma chamber growth during intercaldera periods: Insights from thermo-mechanical modeling with applications to Laguna del Maule, Campi Flegrei, Santorini, and Aso: Geochemistry, Geophysics, Geosystems, v. 20, no. 3, p. 1574–1591, https://doi.org/10.1029/2018GC008103.

Troch, J., Ellis, B.S., Schmitt, A.K., Bouvier, A.-S., and Bachmann, O., 2018, The dark side of zircon: Textural, age, oxygen isotopic and trace element evidence of fluid saturation in the subvolcanic reservoir of the Island Park–Mount Jackson Rhyolite, Yellowstone (USA): Contributions to Mineralogy and Petrology, v. 173, no. 7, https://doi.org/10.1007/s00410-018-1481-2.

Turner, A.J., Katz, R.F., Behn, M.D., and Keller, T., 2017, Magmatic focusing to mid-ocean ridges: The role of grain-size variability and non-Newtonian viscosity: Geochemistry, Geophysics, Geosystems, v. 18, no. 12, p. 4342–4355, https://doi.org/10.1002/2017GC007048.

Vermeesch, P., 2004, How many grains are needed for a provenance study?: Earth and Planetary Science Letters, v. 224, no. 3–4, p. 441–451, https://doi.org/10.1016/j.epsl.2004.05.037.

Vermeesch, P., 2012, On the visualisation of detrital age distributions: Chemical Geology, v. 312, p. 190–194, https://doi.org/10.1016/j.chemgeo.2012.04.021.

von Quadt, A., Gallhofer, D., Guillong, M., Peytcheva, I., Waelle, M., and Sakata, S., 2014, U–Pb dating of CA/non-CA treated zircons obtained by LA-ICP-MS and CA-TIMS techniques: Impact for their geological interpretation: Journal of Analytical Atomic Spectrometry, v. 29, no. 9, p. 1618–1629, https://doi.org/10.1039/C4JA00102H.

Watson, E.B., 1996, Dissolution, growth and survival of zircons during crustal fusion: Kinetic principals, geological models and implications for isotopic inheritance: Earth and Environmental Science Transactions of the Royal Society of Edinburgh, v. 87, no. 1–2, p. 43–56, https://doi.org/10.1017/S0263593300006465.

Watson, E.B., and Harrison, T.M., 1983, Zircon saturation revisited: Temperature and composition effects in a variety of crustal magma types: Earth and Planetary Science Letters, v. 64, no. 2, p. 295–304, https://doi.org/10.1016/0012-821X(83)90211-X.

Weber, G., Caricchi, L., Arce, J.L., and Schmitt, A.K., 2020, Determining the current size and state of subvolcanic magma reservoirs: Nature Communications, v. 11, no. 1, https://doi.org/10.1038/s41467-020-19084-2.

White, L.T., and Ireland, T.R., 2012, High-uranium matrix effect in zircon and its implications for SHRIMP U–Pb age determinations: Chemical Geology, v. 306, p. 78–91, https://doi.org/10.1016/j.chemgeo.2012.02.025.

Widmann, P., Davies, J., and Schaltegger, U., 2019, Calibrating chemical abrasion: Its effects on zircon crystal structure, chemical composition and U-Pb age: Chemical Geology, v. 511, p. 1–10, https://doi.org/10.1016/j.chemgeo.2019.02.026.

Wotzlaw, J.-F., Schaltegger, U., Frick, D.A., Dungan, M.A., Gerdes, A., and Günther, D., 2013, Tracking the evolution of large-volume silicic magma reservoirs from assembly to supereruption: Geology, v. 41, no. 8, p. 867–870, https://doi.org/10.1130/G34366.1.